THE EMISSION-LINE PROPERTIES OF LOW-REDSHIFT QUASI-STELLAR OBJECTS

TODD A. BOROSON AND RICHARD F. GREEN
Kitt Peak National Observatory, National Optical Astronomy Observatories,[1] P.O. Box 26732, Tucson, AZ 85726

ABSTRACT

Spectra covering the region $\lambda\lambda 4300$–5700 have been obtained of all 87 QSOs in the BQS catalog having redshifts less than 0.5. An empirical technique which allows the measurement and subtraction of the many Fe II lines in this region has been developed and applied to these spectra. Measurements of the strengths of Hβ, [O III]$\lambda 5007$, and He II $\lambda 4686$, and a four-dimensional parameterization of the Hβ profile have been combined with optical, radio, and X-ray continuum information from the literature to try to understand how these properties are related.

An analysis including the complete correlation matrix of the measured and compiled properties and a principal component analysis reveal the following results: Most of the variance is connected to two sets of correlations, the first being a strong anticorrelation between measures of Fe II and [O III]. The asymmetry and width of the Hβ line are also associated with this eigenvector. The second group of correlations involves the optical luminosity, the strength of He II $\lambda 4686$, and α_{ox}. The next three eigenvectors are each dominated by a single property: Hβ equivalent width, the shape of the Hβ line, and the shift of the peak of the Hβ line from the systemic velocity.

We conclude (1) the dominant source of variation in the observed properties of low redshift QSOs is a physical parameter which balances Fe II excitation against the illumination of the narrow line region. We argue that this property (and the observed properties of QSOs in general) is not driven by *external* orientation, i.e., our viewing angle, for three reasons. First, the dominant eigenvector is highly correlated with [O III] luminosity, an isotropic property. Second, the steep-spectrum radio sources fall on logical extrapolations of relations defined by the radio-quiet objects, arguing against a distinction in the basic physical parameters driving the observables in the two types of objects. Third, the Fe II lines have the same widths as the Hβ lines, suggesting that they must arise in the same region and have the same degree of anisotropy, a finding inconsistent with the currently popular AGN unification models. Our best guess is that this dominant parameter is related to the fraction of the Eddington luminosity at which the object is emitting. (2) The second parameter is explained as a correlation between luminosity and the slope of the ionizing continuum, in the sense that lower luminosity objects have harder spectra. (3) A comparison of subsamples defined by their radio properties suggests that radio-quiet and radio-loud objects cannot be parallel sequences because there is a large deficit of radio-quiet analogs to the steep-spectrum QSOs. Instead, radio-loud objects should be thought of as the extreme end of some (unknown) property which also determines Fe II and [O III] strength and the asymmetry of the Hβ line. The one significant distinction is that in radio-loud objects the peak of Hβ is systematically shifted to the red, while for radio-quiet objects, there are equal numbers of red- and blueshifts. (4) In confirmation of Sulentic et al. we find no correlation between Hβ asymmetry and centroid shift, indicating that a relativistic accretion disk explanation for the line profiles is not justified in general.

Subject headings: galaxies: Seyfert — quasars: general — surveys

1. INTRODUCTION

Despite the fact that several thousand quasi-stellar objects (QSOs) are now known, there is relatively little agreement on the relations among observable properties. A great many measurements of fluxes in various bands, line strengths, widths, and shapes have been made, but searches for trends in these data have yielded relatively little to constrain models or even to provide clues as to the physical processes which determine these observed characteristics. Many of the relations that have been claimed have become controversial, seen in some data sets but not in others. Theoretical modeling of the radiation

processes in QSOs suggest that the wide range of frequencies over which QSOs are luminous is important; ties between X-ray, optical, infrared, and radio properties have been claimed. To some extent, the fact that QSOs are luminous over such a large range of frequencies (and are visible over such a large range in redshift) is one of the difficulties. One would like to study a complete or at least a representative sample and it is unclear which properties should be chosen as representing minimal selection effects.

Correlations among observed properties not only lead to a physical basis for classification schemes, but, in a field in which even the energy source and mechanism of transport are still argued, can strongly discriminate among competing models. Some of the physical properties which, through models, make predictions about correlations among properties are accretion rate, geometry of the accretion disk, size of the broad line re-

109

gion (BLR), relation between the geometry and the kinemat-
ics of the BLR, orientation of the principal axis with respect to
the line of sight, and mechanism by which energy is trans-
ported to the BLR. Furthermore, correlations with luminosity
might make QSOs viable for cosmological studies; indeed
some studies of QSO properties have been motivated by this
hope (Baldwin, Wampler, & Gaskell 1989).

One of the principal difficulties in evaluating the reality of
correlations seen between observable properties is the problem
of selection effects. Clearly, there is no way to know whether
the differences between a radio-selected sample and an opti-
cally selected sample truly represent differences between radio-
loud and radio-quiet QSOs or are merely indicative of two
different sets of selection effects. A related problem is incom-
pleteness. Many samples are limited to objects known anecdo-
tally to have certain properties (such samples are often referred
to as representative though not complete). For instance, one
could make two lists of QSOs, one with strong Fe II and one
with weak Fe II, and comparison of the two samples may not
reveal anything about the differences between Fe II strong and
Fe II weak objects.

In order to determine the true correlations among observ-
able properties, and try to understand the physical basis for
these correlations, this paper presents a study of the BQS sam-
ple (Schmidt & Green 1983). This is a UV excess, magnitude-
limited sample, and the selection effects which affect it have
been studied by Wampler & Ponz (1985). In short, the color
criterion is not compromised by emission lines at redshifts
below about 0.5, and so we have chosen to limit ourselves to
that range. There was no radio selection criterion, but the en-
tire sample has been observed by Kellermann et al. (1989) who
give 6 cm fluxes. Optical and IR photometry have been pub-
lished by Neugebauer et al. (1987). X-ray observations of a
large fraction of the BQS sample have been published by Tan-
anbaum et al. (1986). We chose to concentrate on the region
around Hβ because of the proximity of a number of interesting
features including Hβ itself, [O III] $\lambda\lambda$4959, 5007, He II λ4686,
and the Fe II complexes on both the blue and red sides of Hβ.
Also, this spectral region is easily accessible up to a redshift
of 0.5.

In § 2, we present a description of the observations and data
reduction technique including a procedure we have developed
for measuring and removing the Fe II contribution indepen-
dent of its velocity broadening. § 3 discusses the correlations
among a compilation of observed properties including those
measured from our spectra and a number of properties at other
wavelengths gathered from the literature. A principal compo-
nent analysis is used to better understand how the correlations
are themselves related. Section 4 contains a discussion of the
results including (1) interpretation of the principal component
analysis, (2) the differences among QSOs with different radio
properties, (3) interpretations of the line asymmetries and
shifts, and (4) implications of the line widths. We conclude in
§ 5 with a description of further observations that could test or
extend some of our conclusions.

2. OBSERVATIONS AND DATA REDUCTION

The sample of objects we have observed consists of all the
BQS objects (Schmidt & Green 1983) having redshifts less

than 0.5. Specifically, there are 89 such objects listed in Table 1
of Schmidt & Green (1983). Two of these have been removed
from the sample—PG 0119+229 because it does not have
broad lines (Keel 1985), and PG 1352+011 because its correct
redshift is $z = 1.121$ (Wampler & Ponz 1985). Note that the
final sample of 87 AGNs includes those objects having abso-
lute magnitudes $M_B > -23$ as well as the more luminous ob-
jects. We will refer to all these objects as QSOs even though
some may not meet a purist's luminosity criterion.

All the observations were made with the KPNO 2.1 m tele-
scope and the Gold Spectrograph, using a TI 800 × 800 CCD
as detector. Two different 300 g mm^{-1} gratings were used,
blazed at λ4000 and λ6750, depending on the redshift of the
source. These gratings give a dispersion of about 2.5 Å pixel^{-1}.
All observations were made through a 1".5 slit which produced
a resolution of 6.5 to 7 Å as measured from the comparison
spectra. An attempt was made to cover the wavelength range
$\lambda\lambda$4300–5700 in the rest frame of each object, but for some of
the higher redshift objects this range had to be trimmed a little
bit. Exposure times were generally between 1800 and 3600 s
depending on the brightness of the object. The slit was posi-
tioned north-south for all observations and we attempted to
observe as close to the meridian as possible. Spectra of compari-
son arcs were obtained frequently throughout each night and
spectrophotometric standard stars were observed at least twice
each night. The standards were used both for flux calibration
and for removal of atmospheric absorption features. All obser-
vations were obtained at airmasses less than 1.5. The spectra
were obtained on a number of nights in 1990 and 1991 and a
log of the observations is given in Table 1. In addition to the
information about the observations listed in Table 1 are some
other properties compiled from the literature. Column (6)
gives an absolute magnitude at λ5500 in the rest frame of each
QSO (which we call M_v), derived from fluxes in Neugebauer et
al. (1987) and calculated assuming H$_0$ = 50 km s^{-1} Mpc^{-1} and
$q_0 = 0.1$. Six of the objects were not observed by Neugebauer et
al. (1987), and for these, we compute M_v from the V-magni-
tudes in Veron-Cetty & Veron (1989) or Hewitt & Burbidge
(1987). Column (7) lists the logarithm of R, the ratio of radio
(6 cm) to optical (4400 Å) flux density as given by Kellermann
et al. (1989). Column (8) designates each object as radio-quiet
(if log $R < 1$), steep radio spectrum (if log $R > 1$ and $\alpha_{2,6} > 0.5$)
where $\alpha_{2,6}$ is the radio spectral index as given by Veron-Cetty &
Veron (1989), or flat radio spectrum (if log $R > 1$ and $\alpha_{2,6} <$
0.5). Column (9) lists the X-ray to optical spectral index, α_{ox},
as given by Tananbaum et al. (1986) or Kriss (1988).

The frames were reduced in the usual way, including bias
subtraction using overclocked pixels in each row, subtraction
of a mean bias frame including a preflash to improve charge
transfer efficiency, and division by a normalized flat field. One
dimensional sky-subtracted spectra were then extracted from
each frame using a spatial width of about 6" centered on the
nucleus. These spectra were wavelength calibrated and re-
binned to a linear dispersion having 2.5 Å per pixel. The spec-
tra were corrected for extinction, flux calibrated, and corrected
for atmospheric absorption features. The redshift of each QSO
was measured by fitting the upper half of the [O III] λ5007 line
to a Gaussian except in the case of eight objects (PG
0043+039, PG 0050+124, PG 1259+593, PG 1402+261, PG
1444+407, PG 1543+489, PG 1700+518, and PG 2112+059)

TABLE 1

OBSERVATIONS OF PG QUASARS

PG QSO (1)	Other Name (2)	z (3)	Date (4)	Exp (5)	M_V (6)	Log R (7)	Radio (8)	α_{ox} (9)
0003+158		0.450	1990 Oct 10	3600	−26.92	2.24	Steep	1.39
0003+199	Mk 335	0.025	1990 Sep 18	500	−22.14	−0.57	Quiet	1.25
0007+106	IIIZw 2	0.089	1990 Sep 18	1200	−23.85	2.29	Flat	1.06
0026+129		0.142	1990 Oct 11	3000	−24.71	0.03	Quiet	1.43
0043+039	PB 6151	0.384	1990 Sep 20	2700	−26.16	−0.92	Quiet	...
0049+171	MK 1148	0.064	1990 Sep 18	1800	−21.81	−0.49	Quiet	1.24
0050+124	I Zw 1	0.061	1990 Sep 19	1200	−23.77	−0.48	Quiet	1.44
0052+251		0.155	1990 Oct 11	3600	−24.64	−0.62	Quiet	1.36
0157+001	Mk 1014	0.164	1990 Oct 11	3600	−24.61	0.33	Quiet	1.68
0804+761		0.100	1990 Feb 16	750	−24.44	−0.22	Quiet	1.34
0838+770		0.131	1990 Feb 17	2400	−23.83	−0.96	Quiet	1.57
0844+349	Ton 951	0.064	1990 Feb 15	1300	−23.31	−1.52	Quiet	1.53
0921+525	MK 110	0.035	1990 Feb 15	1800	−21.25	0.17	Quiet	...
0923+201	TON 1057	0.190	1990 Feb 15	1800	−24.56	−0.85	Quiet	1.41
0923+129	MK 705	0.029	1990 Feb 17	2400	−21.59	0.32	Quiet	1.58
0934+013		0.050	1990 Apr 21	3600	−21.43	−0.42	Quiet	1.29
0947+396	K347-45	0.206	1991 Apr 23	3600	−24.21	−0.60	Quiet	...
0953+414	K348-7	0.239	1990 Feb 19	1800	−25.65	−0.36	Quiet	...
1001+054		0.161	1990 Feb 18	3200	−24.07	−0.30	Quiet	1.78
1004+130	4C 13.41	0.240	1990 Apr 21	3600	−25.97	2.36	Steep	1.92
1011−040		0.058	1990 Feb 15	1800	−22.70	−1.00	Quiet	1.93
1012+008		0.185	1990 Feb 17	2400	−24.79	−0.30	Quiet	...
1022+519	MK 142	0.045	1990 Feb 16	1800	−21.40	−0.64	Quiet	1.46
1048+342		0.167	1990 Feb 16	3600	−24.02	−1.00	Quiet	...
1048−090	3C 246	0.344	1990 Apr 22	2620	−25.83	2.58	Steep	1.41
1049−005		0.357	1991 Feb 15	2500	−25.93	−0.60	Quiet	...
1100+772	3C 249.1	0.313	1990 Feb 19	1951	−25.86	2.51	Steep	1.36
1103−006	PKS	0.425	1991 Apr 23	3600	−25.96	2.43	Steep	...
1114+445		0.144	1990 Feb 16	2700	−24.01	−0.89	Quiet	...
1115+407		0.154	1990 Feb 18	3592	−23.74	−0.77	Quiet	...
1116+215	TON 1388	0.177	1991 Apr 23	1500	−25.57	−0.14	Quiet	1.45
1119+120	MK 734	0.049	1990 Feb 16	600	−22.49	−0.82	Quiet	1.55
1121+422		0.234	1990 Feb 19	3600	−24.38	−1.00	Quiet	...
1126−041	MK 1298	0.060	1990 Feb 15	1600	−23.00	−0.77	Quiet	1.90
1149−110		0.049	1990 Feb 16	1800	−21.90	−0.06	Quiet	...
1151+117		0.176	1990 Feb 17	3600	−24.07	−1.15	Quiet	...
1202+281	GQ COM	0.165	1990 Feb 20	3600	−23.75	−0.72	Quiet	1.42
1211+143		0.085	1990 Feb 15	750	−24.60	1.39	Steep	1.22
1216+069		0.334	1990 Apr 22	3600	−26.33	0.22	Quiet	1.53
1226+023	3C 273	0.158	1990 Feb 16	900	−27.15	3.06	Flat	1.32
1229+204	TON 1542	0.064	1990 Apr 21	2400	−23.06	−0.96	Quiet	1.47
1244+026		0.048	1990 Feb 15	3200	−21.77	−0.28	Quiet	1.23
1259+593	LB 2522	0.472	1991 Apr 22	3600	−26.82	−1.00	Quiet	...
1302−102	PKS	0.286	1990 Apr 21	2000	−26.60	2.27	Flat	1.49
1307+085		0.155	1991 Apr 23	2000	−24.56	−1.00	Quiet	1.40
1309+355	TON 1565	0.184	1991 Apr 24	2700	−24.76	1.26	Flat	...
1310−108		0.035	1990 Feb 16	1800	−21.35	−1.00	Quiet	1.37
1322+659		0.168	1990 Feb 20	2500	−24.23	−0.92	Quiet	...
1341+258	TON 730	0.087	1991 Apr 24	3000	−22.71	−0.92	Quiet	...
1351+236	MK 662	0.055	1991 Apr 24	4800	−22.40	−0.59	Quiet	...
1351+640		0.087	1990 Feb 15	1000	−24.08	0.64	Quiet	1.91
1352+183	PB 4142	0.158	1990 Feb 20	3000	−24.13	−0.96	Quiet	1.41
1354+213		0.300	1990 Apr 22	3600	−24.34	−1.10	Quiet	...
1402+261	TON 182	0.164	1990 Feb 20	2400	−24.48	−0.64	Quiet	1.55
1404+226		0.098	1990 Feb 16	2000	−22.93	−0.33	Quiet	1.79
1411+442	PB 1732	0.089	1990 Feb 15	1800	−23.54	−0.89	Quiet	...
1415+451		0.114	1990 Feb 20	3000	−23.41	−0.77	Quiet	...
1416−129		0.129	1990 Feb 17	1800	−24.55	0.06	Quiet	1.38
1425+267	TON 202	0.366	1991 Apr 23	3600	−26.18	1.73	Steep	1.68
1426+015	MK 1383	0.086	1990 Feb 15	1000	−24.05	−0.55	Quiet	1.26
1427+480		0.221	1991 Apr 23	3000	−24.04	−0.80	Quiet	...
1435−067		0.129	1990 Feb 17	1800	−24.10	−1.15	Quiet	1.40
1440+356	MK 478	0.077	1990 Feb 15	1600	−23.49	−0.43	Quiet	...
1444+406		0.267	1991 Apr 23	3000	−25.18	−1.10	Quiet	...
1448+273		0.065	1990 Feb 15	1350	−23.30	−0.60	Quiet	...
1501+106	MK 841	0.036	1990 Feb 15	600	−22.76	−0.44	Quiet	1.16
1512+370	4C 37.43	0.371	1990 Sep 20	2700	−25.93	2.28	Steep	...
1519+226		0.137	1990 Feb 20	3600	−23.76	−0.05	Quiet	1.48
1534+580	MK 290	0.030	1990 Feb 16	2400	−21.44	−0.15	Quiet	1.27
1535+547	I Zw 120	0.038	1990 Feb 15	1400	−22.15	−0.85	Quiet	...
1543+489		0.400	1990 Sep 20	2400	−25.60	−0.82	Quiet	...

TABLE 1—*Continued*

PG QSO (1)	Other Name (2)	z (3)	Date (4)	Exp (5)	M_V (6)	Log R (7)	Radio (8)	α_{ox} (9)
1545+210	3C 323.1	0.266	1990 Sep 19	2400	−25.63	2.62	Steep	1.28
1552+085		0.119	1990 Feb 17	2400	−23.72	−0.35	Quiet	1.69
1612+261	TON 256	0.131	1990 Apr 23	2000	−23.77	0.45	Quiet	1.33
1613+658	MK 876	0.129	1990 Apr 23	3600	−24.22	0.00	Quiet	1.47
1617+175	MK 877	0.114	1990 Feb 20	1400	−23.95	−0.14	Quiet	1.52
1626+554		0.133	1990 Apr 23	3000	−23.54	−0.96	Quiet	...
1700+518		0.292	1990 Sep 19	2400	−26.44	0.37	Quiet	...
1704+608	3C 351	0.371	1990 Sep 20	2423	−26.38	2.81	Steep	1.60
2112+059		0.466	1990 Oct 10	3000	−27.26	−0.49	Quiet	1.82
2130+099	II Zw136	0.061	1990 Sep 18	1000	−23.23	−0.49	Quiet	1.46
2209+184		0.070	1990 Sep 18	600	−23.14	2.15	Flat	1.35
2214+139	MK 304	0.067	1990 Sep 18	500	−23.39	−1.30	Quiet	1.83
2233+134		0.325	1990 Oct 10	3600	−25.18	−0.55	Quiet	1.64
2251+113	PKS	0.323	1990 Oct 11	3600	−26.24	2.56	Steep	1.80
2304+042	PB 5250	0.042	1990 Sep 18	600	−21.58	−0.60	Quiet	...
2308+098	4C 09.72	0.432	1990 Oct 10	3600	−26.24	2.27	Steep	...

NOTES.—Col. (1), PG designation of QSO. Col. (2), Name in other catalogs. Col. (3), Redshift from Schmidt & Green 1983. Col. (4), Date of observation. Col. (5), Exposure time in s. Col. (6), Absolute monochromatic magnitude at $\lambda5500$ in the rest frame derived from fluxes in Neugebauer et al. 1987 or V-magnitudes (for six objects) listed in Hewitt & Burbidge 1987 or Veron-Cetty & Veron 1989 using $H_0 = 50$ km s^{-1} Mpc^{-1} and $q_0 = 0.1$. Col. (7), logarithm of R, the ratio of radio-to-optical luminosity as tabulated by Kellerman et al. 1989. Col. (8), radio class—Quiet, Steep, or Flat depending on log R and radio spectral index. Col. (9), X-ray to optical spectral index from Tananbaum et al. 1986 or from Kriss 1988.

for which Hβ was used because $\lambda5007$ was weak or absent. The spectra were deredshifted by dividing the two numbers which define the wavelength scale, the starting wavelength and the pixel width in Å, by $(1 + z)$. Because of this procedure, line widths and equivalent widths measured from these deredshifted spectra will correctly refer to the rest frame of the object. The final spectra of the 87 objects in the complete sample are shown in Figure 1. In each plot the uppermost line is the observed spectrum. The plots are in units of 10^{-16} ergs cm^{-2} s^{-1} Å^{-1} observed against rest wavelength in Å.

It is clear from inspection of Figure 1 that the Fe II emission is a complicating factor in measuring widths and strengths of spectral features. It can be seen in many of the spectra as two broad humps at $\lambda\lambda4450–4700$ and $\lambda\lambda5150–5350$. In addition there is a strong multiplet (42) consisting of three lines at $\lambda\lambda4924, 5018, 5169$. These lines make the measurement of the [O III] $\lambda\lambda4949,5007$ lines difficult, in particular when the [O III] lines are weak. Even determining the strength of the Fe II emission itself is not straightforward; there are so many lines present that, as the velocity broadening increases, the points that one might pick to fix the level of the continuum are more and more contaminated by Fe II emission (Wills & Browne 1986). Instead of adopting points to define the continuum level, measuring the Fe II equivalent width, and then correcting for such contamination (Boroson, Persson, & Oke 1985), we have developed a new technique which allows us to measure and remove the Fe II from the spectrum.

We begin with a spectrum of PG 0050+124 (I Zwicky 1), an object which is remarkable both for the strength of its Fe II emission and for the narrowness of its "broad lines." This object has been well studied by Phillips (1978) and Oke & Lauer

(1979) who identify a great many of the features between $\lambda3500$ and $\lambda7000$ with Fe II transitions. Our approach was to make a template Fe II spectrum by removing the lines which are *not* Fe II from the spectrum of I Zw 1. Then we generated a two parameter family of Fe II spectra, defined by line width and line strength and compared these spectra to the features in each object. Note that this procedure assumes that the relative strengths of the lines (both within each multiplet and among multiplets) is the same in all objects. We have satisfied ourselves that this is at least approximately true by comparing the relative peaks of the individual Fe II lines in I Zw 1 with the peaks in some of the other spectra with relatively narrow lines.

In order to pursue this approach, we obtained a high signal-to-noise spectrum using several different grating tilts of I Zw 1 covering the range $\lambda\lambda3600–7200$. These observations were made with the same instrumentation as those of all the other objects so that the instrumental resolution is the same. The extended wavelength coverage is necessary to avoid edge effects when simulating large velocity dispersions. The reduced spectrum was rebinned to a log wavelength scale and the continuum was subtracted by fitting a low order polynomial to the regions between obvious emission lines. Using this, a typical broad line profile was generated from the Hα line after removing the small contributions from [N II] $\lambda\lambda6548, 6583$ and several weak Fe II lines on the blue wing of Hα. This broad-line profile was then scaled and shifted in log wavelength to subtract the contributions of Hβ and Hγ. Because the forbidden lines may have slightly different widths than the permitted lines in I Zw 1 (Oke & Lauer 1979), we chose to subtract the [O III] lines and the [N II] $\lambda5755$ line by hand, smoothly interpolating between the lines on either side. We also subtracted by

hand the feature which is a mix of Na I D and He I λ5876. This feature is well outside the spectral region we have observed in most of the program objects. Finally, we removed the two strongest [Fe II] lines at λ5158 (18F and 19F) and λ5273 (18F). These lines are quite obviously present in I Zw 1 and are not present in the other objects which have strong narrow Fe II emission. The result of this procedure was a spectrum representing only the permitted Fe II emission in I Zw 1.

We then constructed a two-dimensional sequence of spectra in which we broadened the template by convolving with a Gaussian of various widths and by multiplying the spectrum by a scalar factor. These spectra were rebinned back to a scale linear in wavelength and combined into a three-dimensional image—one dimension being wavelength, one being line width, and one being line strength. We found that a series of 30 different widths from the intrinsic full width at half-maximum (FWHM) of I Zw 1 of 900 km s^{-1} up to a FWHM of 8000 km s^{-1} and that a series of 30 different strengths from $\frac{1}{20}$ of the observed I Zw 1 flux to two times the observed flux was sufficient to fit all objects in strength and width. The fitting was then done by eye; each spectrum was expanded into a three dimensional image to match the Fe II template cube and the template cube was then subtracted. Inspection of the difference cube by looking at cuts representing different line widths and strengths showed fairly unambiguously which pair of indices is the best match. In general a successful fit showed a flat continuum between Hγ and He II λ4686 (although He II λ4471 is seen in a few objects). In no case did the line width differ significantly from the width measured for Hβ. *Thus, there is no evidence that the* Fe II *emission arises anywhere other than the same clouds which produce* Hβ. As pointed out by Joly (1991), this is inconsistent with the interpretation, within the framework of beaming models, that differing amounts of anisotropy must be present in the two lines (Jackson & Browne 1991).

From each object the best-fit Fe II spectrum was subtracted. These Fe II spectra and the resulting Fe II subtracted spectra are shown in Figure 1. Note that the Fe II subtracted spectra have been offset downward for visibility. In a few cases even the weakest Fe II emission in our template was obviously too much, and so we interpret this as indicating no detectable Fe II in these objects. These are apparent in Figure 1 because only a single spectrum is shown. The degree to which the Fe II appears to have been successfully subtracted varies from object to object. Since we don't a priori know what is underneath the Fe II, we shall try to interpret the remaining features after subtraction of the Fe II model in terms of other ions. Certainly, in some of the objects, e.g., PG 0003+199, PG 0844+349, PG 1119+120, PG 1322+659, PG 1617+175, the Fe II model appears to fit very well. In other objects, e.g., PG 0804+761, PG 0953+414, PG 1115+407, PG 1116+215, PG 1352+183, PG 1435−067, PG 1626+554, it looks as if Fe II multiplet 42 might be stronger relative to the other multiplets than in I Zw 1 and some residual emission from these strong lines are left in the subtracted spectrum. Note that this modeling technique allows an estimate of the Fe II strength *independent of the line width* since we can measure the flux in the unbroadened Fe II template spectrum, and we know the scaling factor.

The final step in the processing of the spectra was to remove the continuum from each object. This was done by fitting a low order polynomial to the regions which seemed to be uncontaminated by emission lines—generally the portions of the spectrum which had been contaminated by Fe II originally. From each fit, the continuum level at the position of Hβ, λ4861, was tabulated. All equivalent width measurements in this paper refer to the continuum at that point. In order to look at the statistical properties of a uniform set of data, we list in Table 2 the following items which we measured from these spectra. Column (2) lists the equivalent width of Hβ, including both broad and narrow components. It should be noted that in the cases where a distinct narrow component is visible, its contribution is rarely more than 3% of the total Hβ flux. Column (3) lists the equivalent width of [O III] λ5007. Column (4) lists the equivalent width of He II λ4686. Column (5) lists the equivalent width of the Fe II complex between λ4434 and λ4684 (as measured from the model). Column (6) lists the uncertainty in the Fe II measurement. These uncertainties are subjective and contain contributions from the noise in the data and the degree to which the model fits the Fe II emission in that particular object. They should be considered as the 3 σ uncertainty, the point at which the fit becomes obviously incorrect, including both systematic and random errors. The next three columns, (7), (8), and (9), list the ratios of the equivalent widths of [O III] λ5007, He II λ4686, and the Fe II complex to that of Hβ. We denote these ratios R λ5007, R λ4686, and R Fe II. Column (10) lists the ratio of the peak height of the [O III] λ5007 line to that of Hβ (Peak λ5007). Although this quantity is more difficult to interpret than equivalent widths or their ratios, we discovered that it is more closely related to one's subjective impression of the relative strengths of the two lines. The last four columns list the properties which define the Hβ line profile. In each spectrum the width and centroid at $\frac{1}{4}$, $\frac{1}{2}$, and $\frac{3}{4}$ maximum of the broad component of Hβ were measured. Column (11) lists the FWHM of the broad component of the line. Column (12) lists the shift of the centroid at $\frac{3}{4}$ maximum from the rest wavelength in units of the FWHM. Note that we have chosen to define the rest frame of each object from the measured wavelength of its [O III] λ5007 line. Typically these determinations are accurate to 0.5 Å or 30 km s^{-1}, as determined from the spectra which have narrow components of Hβ. The larger uncertainty in the shift (and other profile) values comes from noise in the broad Hβ profile and amounts to approximately 0.01 in the shift parameter. This shift is not tabulated for those objects which do not have measurable [O III]. Column (13) lists a parameter, shape = (FW1/4M+ FW3/4M)/FWHM. Column (14) lists a line asymmetry parameter, Hβ asymm, defined by De Robertis (1985). It is a measure of the shift between the centroids at $\frac{1}{4}$ and $\frac{3}{4}$ maximum in units of the FWHM. It is defined in the sense that a profile which has excess light in its blue wing has a positive value and a profile which has excess light in its red wing has a negative value. Finally, column (15) lists a λ5007 absolute magnitude, $M_{[O III]}$, defined as $M_v - 2.5 \log (EW \lambda5007)$.

3. CORRELATIONS AMONG PROPERTIES

Having measured and tabulated a number of emission-line and continuum properties for this complete sample of QSOs, we now proceed to determine which features are correlated. In practice we approached this by computing the correlation ma-
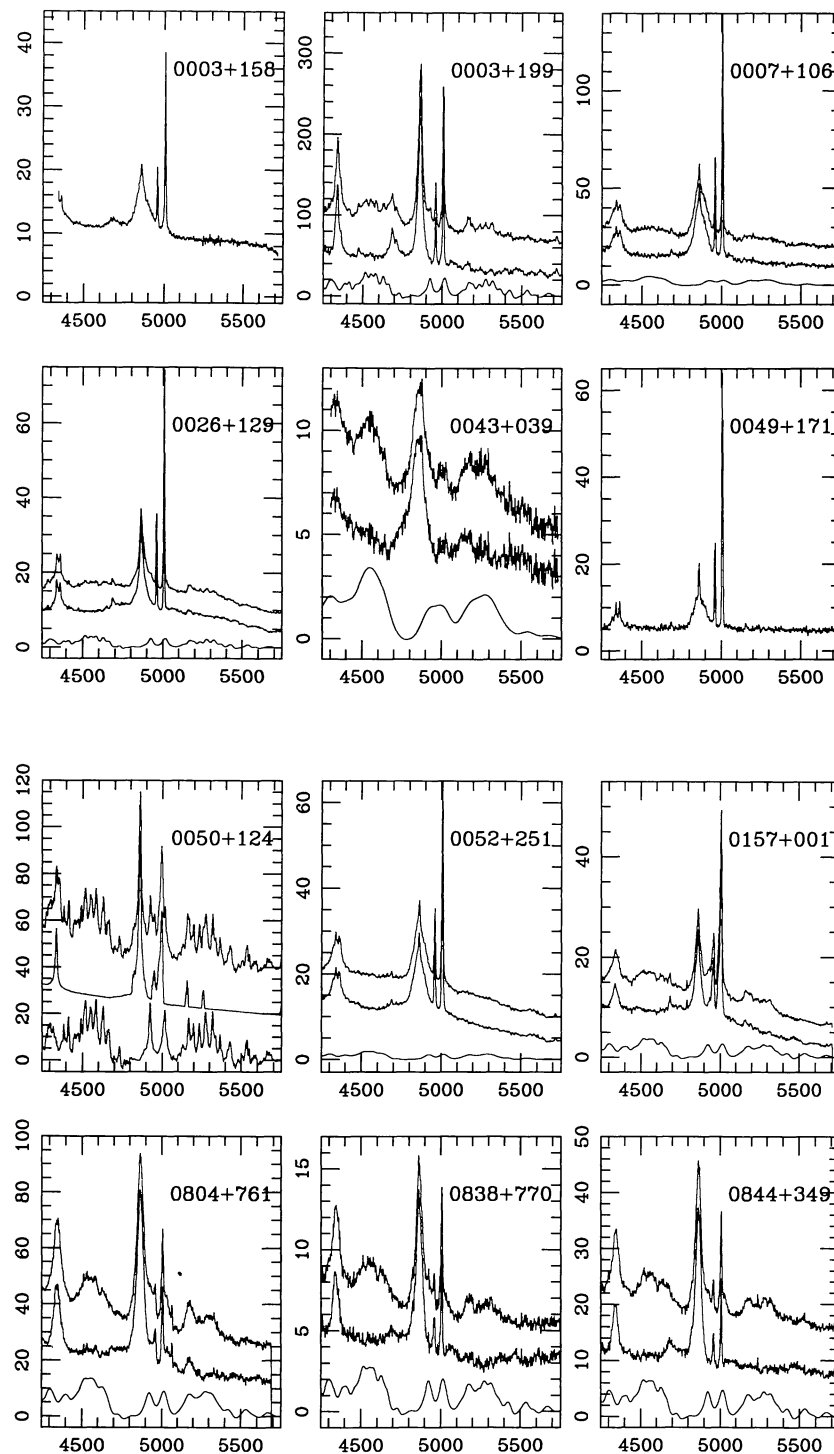
FIG. 1.—Final reduced spectra of the 87 objects which comprise the complete sample. The vertical axis shows observed flux in units of 10^{-16} ergs cm^{-2} s^{-1} Å^{-1}. The horizontal axis is wavelength in Å in the rest frame of the object. For most objects, three spectra are plotted. The top one is the observed spectrum. The bottom one is the Fe II model adopted for that object. The middle one is the Fe II subtracted spectrum shifted downward an arbitrary amount. For seven objects, no Fe II could be detected and only a single spectrum is plotted.
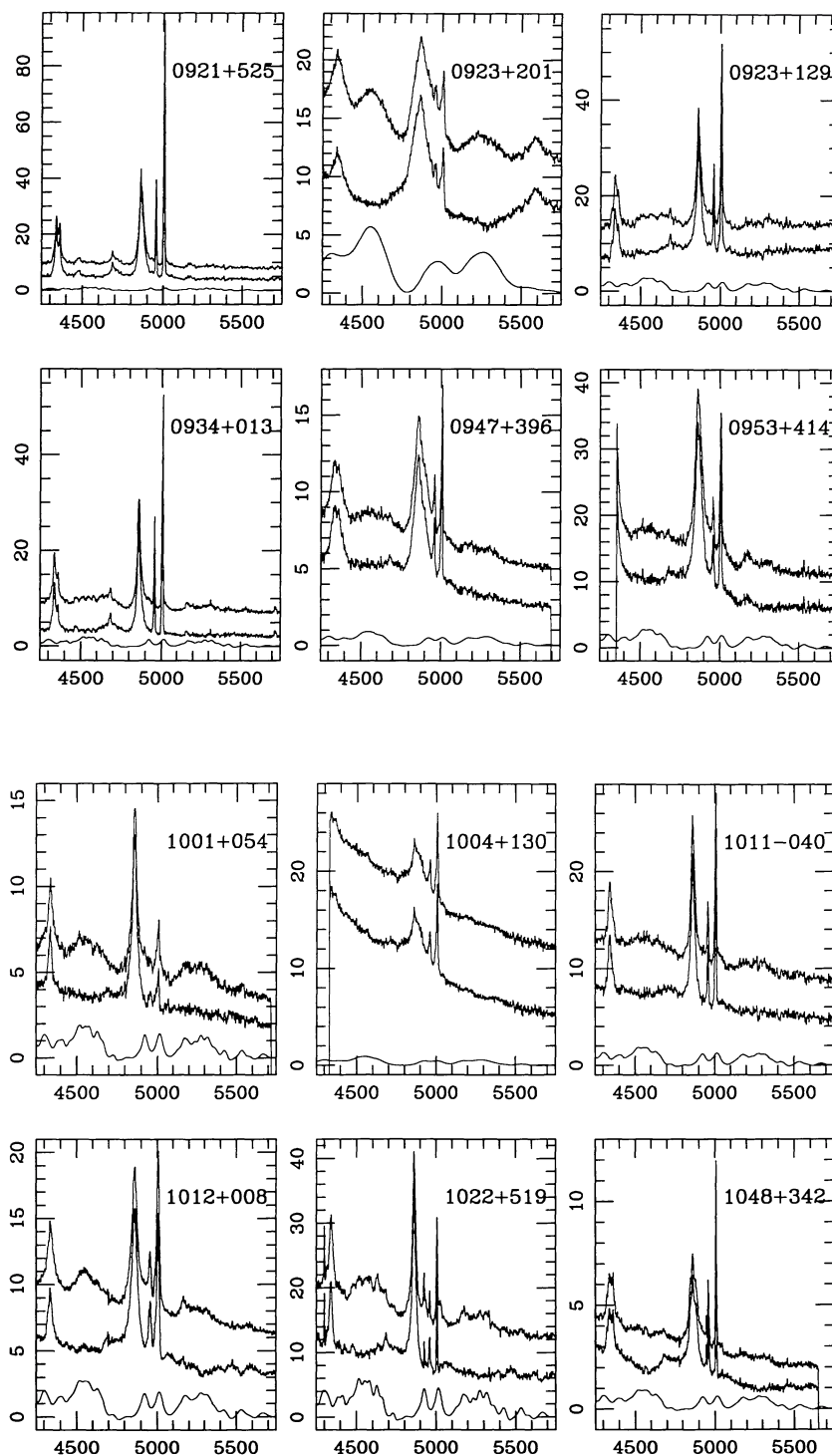
FIG. 1—*Continued*

trix including items 3, 6, 7, and 9 from Table 1, and all items from Table 2 except the Fe II uncertainty. Because the lack of correlation is as interesting in some cases as the strength of correlation in others, we present in Table 3 the complete correlation matrix, with columns and rows labeled as in Tables 1 and 2. Each correlation coefficient (r) is computed using only the objects for which both values are tabulated; all 87 objects are used except in the following cases. Those involving α_{ox} only use the 55 objects for which that parameter is tabulated and those involving Hβ shift only use the 80 objects for which that

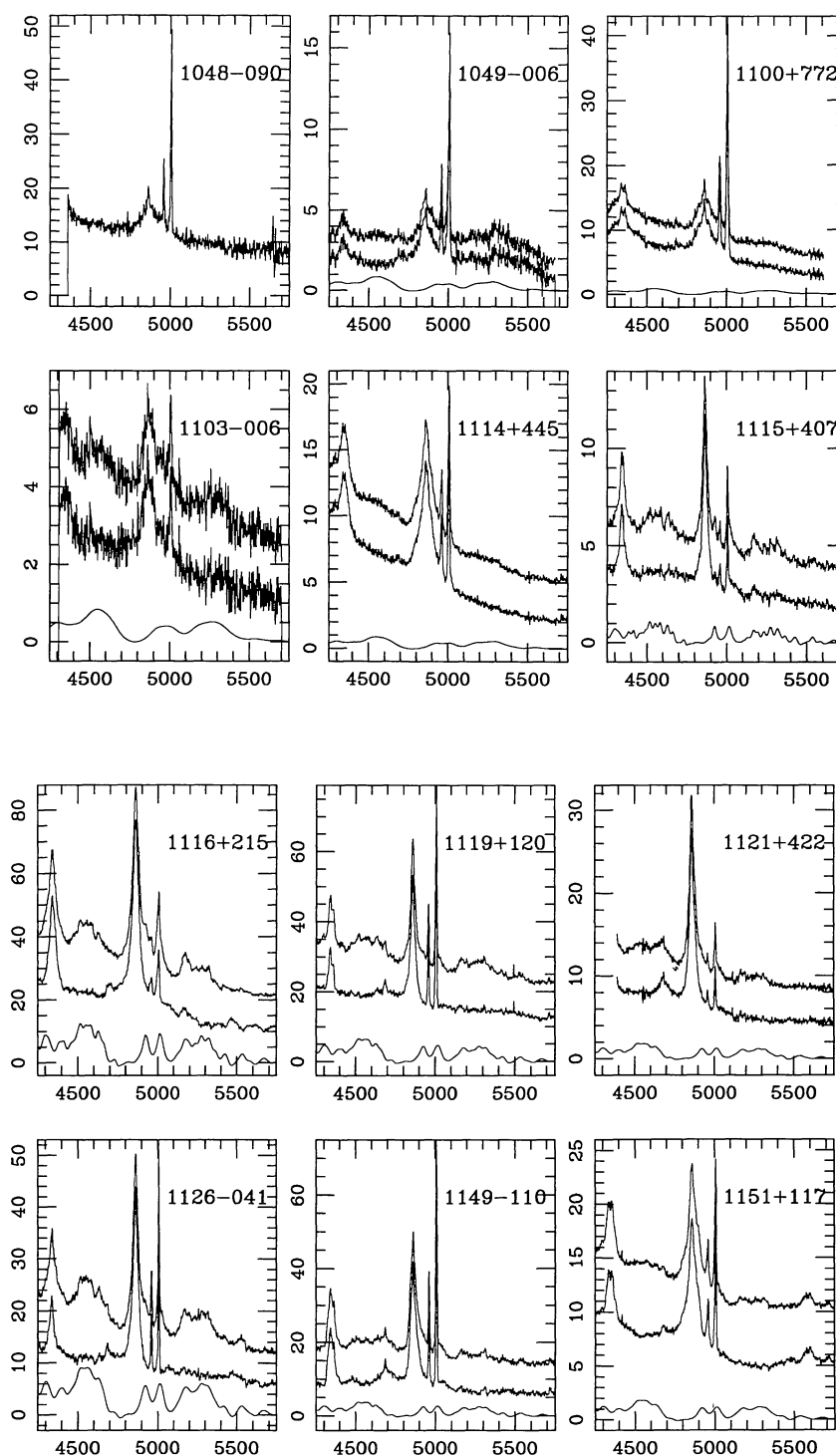FIG. 1—*Continued*

parameter is given. The correlation coefficient relating α_{ox} and Hβ shift uses the 52 objects for which both properties are known.

As a measure of the significance of the correlations, a correlation coefficient value larger than 0.275 is found from un-correlated samples of 87 objects with 1% probability. We have examined 17 properties yielding $17 \times \frac{16}{2} = 136$ correlation coefficients. One might expect one or two coefficients larger than 0.275 by chance out of these 136. In fact, 57 coefficients are larger than 0.275. Some fraction of these significant corre-
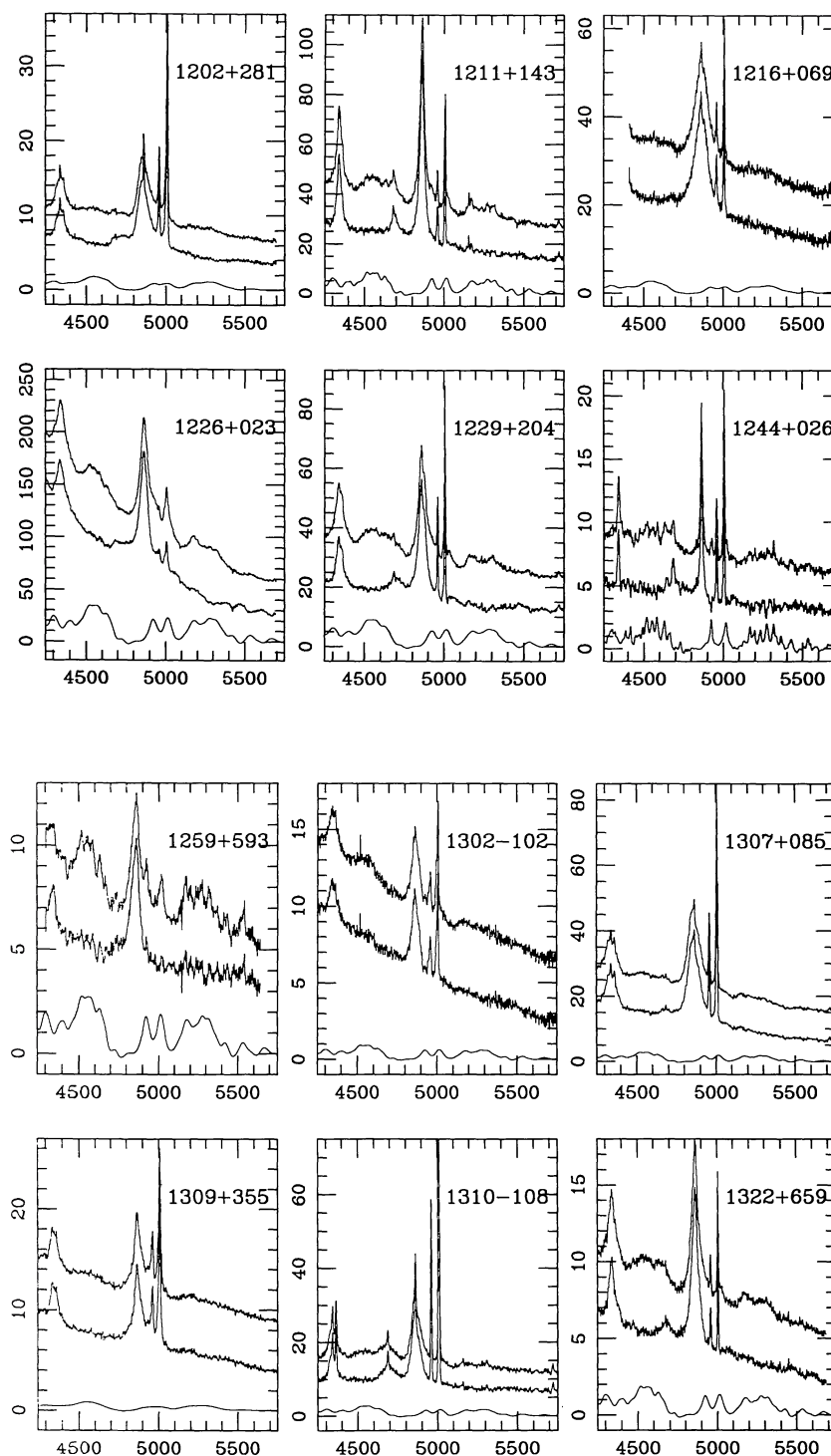
LOW-REDSHIFT QUASARS

FIG. 1—*Continued*

lations are due to selection effects and the fact that we have chosen to measure essentially the same properties in somewhat different ways. For example, z and M_v are correlated ($r = -0.871$) because the sample is limited by apparent magnitude. And R $\lambda5007$, R $\lambda4686$, and R Fe II are correlated with EW

$\lambda5007$, EW $\lambda4686$, and EW Fe II, respectively ($r = 0.803$, 0.876, 0.766) because EW Hβ does not vary much compared to the other lines. Still, when these anomalous correlations are removed, a large number of interesting correlations remain.

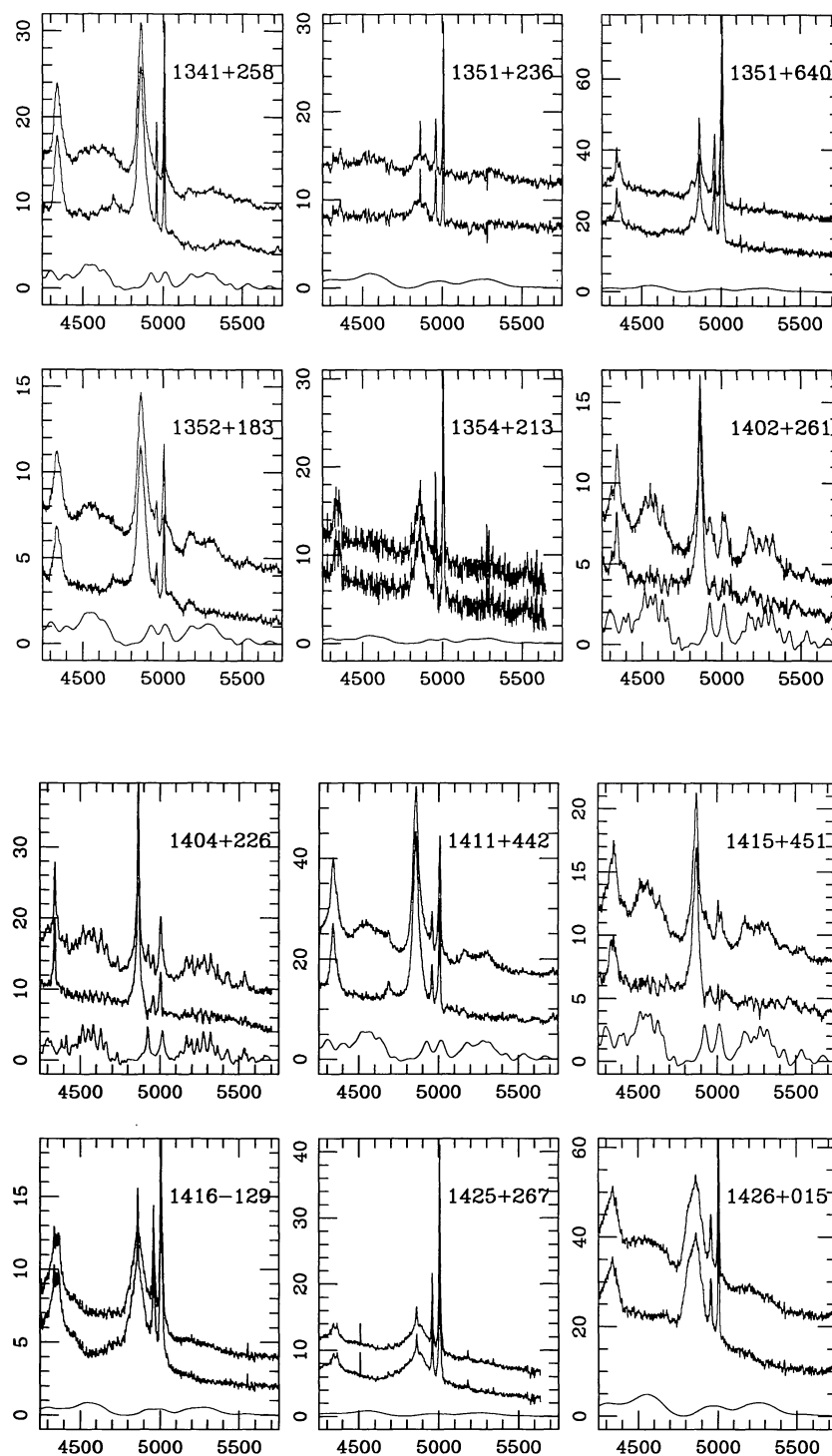The fact that many of the properties are correlated makes

FIG. 1—*Continued*

understanding the physical mechanisms driving the correlations difficult to discern. In order to sort the correlations into meaningful groups we ran a principal component analysis program on the correlation matrix. In simple terms, a new coordinate system is defined in which each successive coordinate direction, defined by the eigenvectors, explains as much of the remaining variance in the data as is possible. Because of the "false correlations," due to selection effects or closely related variables, we experimented with including different subsets of the variables in the principal component analysis. The concern
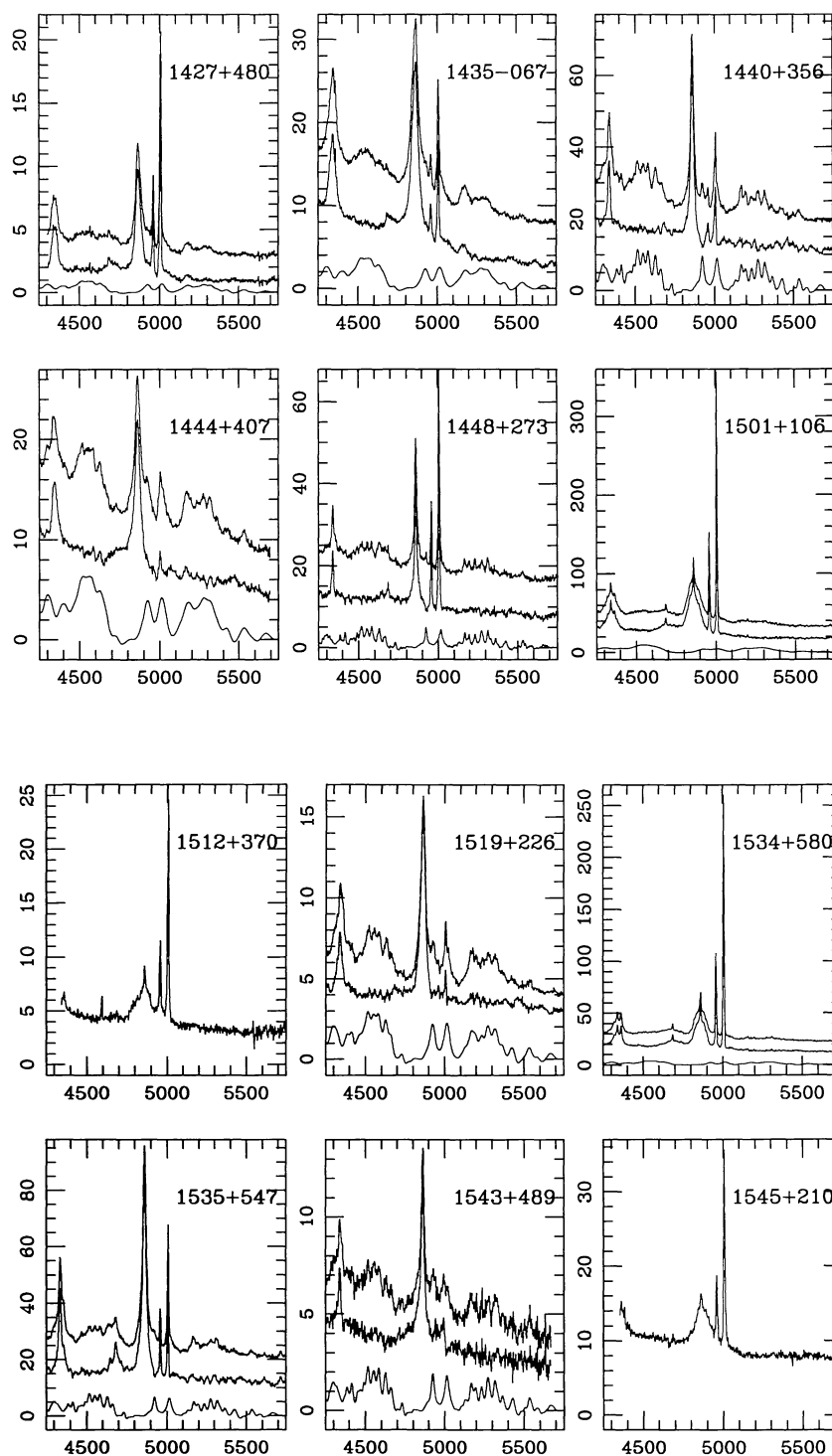
FIG. 1—*Continued*

is that the variance will be dominated by a large number of variables all measuring, say, the scatter in Hβ. We found that essentially the same eigenvectors came out of the analysis whether we included all the variables or the most restricted subset. Thus, we choose to present the principal component

analysis done with 13 of the tabulated properties, M_v, log R, α_{ox}, EW Hβ, R λ5007, R λ4686, R Fe II, Peak λ5007, Hβ FWHM, Hβ shift, Hβ shape, Hβ asymmetry, and $M_{[O III]}$, each of which contains potentially unique information.

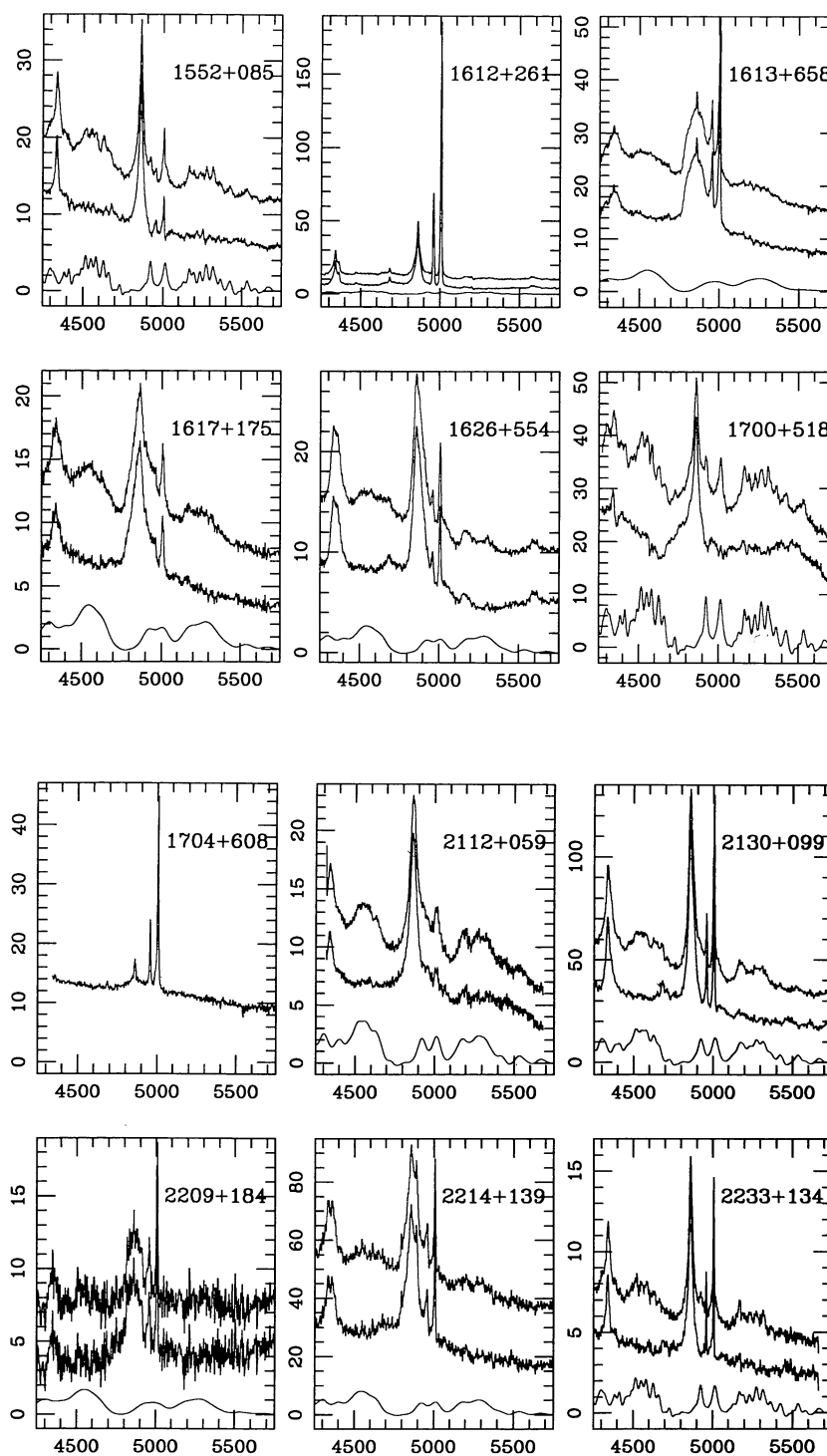We present the results of this analysis in Table 4 which lists

FIG. 1—*Continued*

the five most significant eigenvectors in terms of their projections upon the original 13 properties. At the top of each column the cumulative percentage of the variance accounted for by the eigenvectors up to that point is given. While this sort of approach sometimes obscures the details of what is going on,

in this case it presents a remarkably clear picture of how the properties are related.

In trying to make sense of the eigenvector projections, one can ask which eigenvector correlates most closely with each property. Some of the properties are closely associated with
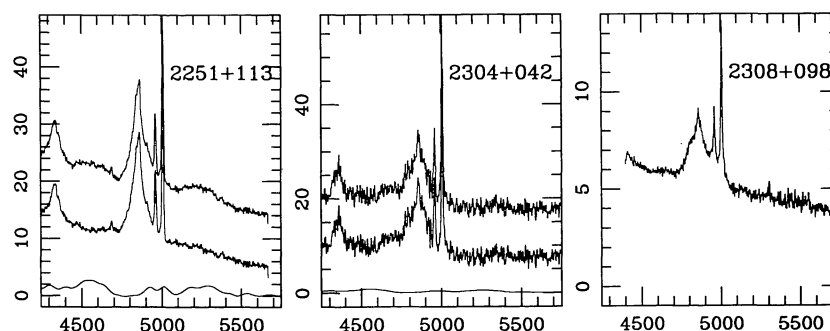
FIG. 1—*Continued*

one of the eigenvectors; Peak $\lambda5007$, for example, has a projection of 0.845 on eigenvector 1 while the next highest projection it has is only -0.270 on eigenvector 3. Other properties, however, are only slightly better associated with one eigenvector than another. Log R, for example has a correlation of 0.566 with eigenvector 1 but -0.404 with eigenvector 3. If we consider the correlations in this way, we find that in the first five eigenvectors, each property is associated with an eigenvector with a projection greater (in absolute value) than 0.5. To then turn this analysis around, one sees that eigenvector 1 is dominated by the anticorrelation between the strength of Fe II and the strength of [O III] $\lambda5007$. In addition, this eigenvector has significant correlation with log R, Hβ FWHM, and Hβ asymmetry. Eigenvector 2 relates He II $\lambda4686$ to optical luminosity in the sense that more luminous objects have weaker He II $\lambda4686$ emission. Each of eigenvectors 3, 4, and 5 is strongly dominated by a single property—EW Hβ, Hβ shape, and Hβ shift, respectively.

3.1. *Eigenvector 1: the* Fe II–[O III] *Anticorrelation*

The principal component analysis indicates that the largest amount of the variance is caused by the strengths of the Fe II and [O III] lines which are strongly anticorrelated. The largest correlation coefficient ($r = -0.670$) occurs for EW Fe II and Peak $\lambda5007$, a plot of which is shown in Figure 2, although all the correlations between the four measures of [O III] and the two measures of Fe II are quite significant. It is of some interest to understand why the strongest correlation is with the ratio of peak heights of the two lines, Hβ and $\lambda5007$ rather than with some parameter more directly connected to the [O III] flux. This peak ratio was initially measured for all the objects because it seemed to represent a better estimate of a subjective impression of the relative strengths of [O III] and Hβ than did the equivalent width ratio. The spectra only barely resolve the narrow lines so the height of the $\lambda5007$ peak is quite closely proportional to the flux in the line. In the case of Hβ, however, the peak height depends equally on the flux (or equivalent width) and on the width of the line. Because equivalent width is not strongly correlated with FWHM (see Table 3), the peak height of Hβ is smaller for relatively broad lines and larger for relatively narrow lines. Thus, Peak $\lambda5007$ represents two different properties, the strength of the [O III] emission and the width of the permitted lines. This is additionally demonstrated

by the significant correlation ($r = 0.508$) between Peak $\lambda5007$ and Hβ FWHM.

That there really are two effects here is demonstrated in Figure 3, in which EW $\lambda5007$ is plotted against eigenvector 1. In this diagram the point representing each object is scaled according to the Hβ FWHM. Thus, the largest points represent the broadest lines. It can be seen that while, in general, EW $\lambda5007$ and Hβ FWHM increase with eigenvector 1, the objects which have stronger $\lambda5007$ at a given value of eigenvector one have smaller Hβ FWHM values. This is confirmed by an analysis of the residuals; if the EW$\lambda5007$ residuals from a least-squares fit to eigenvector 1 are compared with the FWHM values, they are correlated at the 99.5% level. One possible explanation of this phenomenon is that the FWHM measured in objects with narrower profiles has been underestimated because of the presence of a strong narrow-line region. While any obvious narrow Hβ emission was removed before the profile parameters were determined, the narrow Hβ contribution may smoothly blend into the broad-line profile in some cases, causing us to include it in the measured line width.

The nature of the Fe II emission has been much discussed in the literature especially with regard to radio and X-ray properties. While it was noted some time ago that Fe II was stronger in radio quiet QSOs and Seyfert galaxies than in radio loud QSOs and radio galaxies (Osterbrock 1977; Phillips 1977), it was first pointed out by Setti & Woltjer (1977) that Fe II was frequently seen in flat-spectrum radio source QSOs but not in steep-spectrum radio objects. This point has been controversial as some studies (Bergeron & Kunth 1984) do not find a difference between steep spectrum (extended morphology) and flat spectrum (compact morphology) objects while others (Miley & Miller 1979; Steiner 1981; Boroson & Oke 1984) do. Similarly, an inverse correlation between the strength of Fe II and forbidden line emission has been proposed (Phillips 1977) but discounted because of the existence of 3C 48 which has both strong Fe II and strong forbidden lines. This large, complete sample shows unequivocally that Fe II is strong in objects with weak [O III] emission and weak in those with strong [O III] emission. The existence of correlations regardless of whether the measurements are referenced to the continuum, Hβ flux, or Hβ height leave no doubt that this is a real effect.

Because much of the controversy over Fe II has involved radio properties, we next turn to these. The use of log R as an indicator of radio luminosity requires some additional explana-

TABLE 2
EMISSION-LINE PROPERTIES

PG QSO (1)	EW Hβ (2)	EW λ5007 (3)	EW λ4686 (4)	EW Fe II (5)	σ_FeII (6)	R λ5007 (7)	R λ4686 (8)	R Fe II (9)	Peak λ5007 (10)	Hβ FWHM (11)	Hβ shift (12)	Hβ shape (13)	Hβ asymm (14)	M[OIII] (15)
0003+158	91	26	14.4	0	17	0.28	0.16	0.00	2.70	4760	-.046	1.143	-0.163	-30.44
0003+199	95	22	26.8	59	4	0.23	0.28	0.62	0.80	1640	-.043	1.198	+0.068	-25.49
0007+106	101	42	1.7	35	7	0.42	0.02	0.35	3.07	5100	+.018	1.050	-0.046	-27.91
0026+129	65	29	7.4	33	11	0.45	0.11	0.51	2.68	1860	+.089	1.285	-0.143	-28.37
0043+039	92	1	0.0	109	27	0.01	0.00	1.18	0.12	5300	-.130	1.255	+0.149	-26.16
0049+171	136	97	4.6	0	30	0.72	0.03	0.00	3.99	5250	+.021	1.058	-0.047	-26.78
0050+124	51	22	0.0	75	5	0.43	0.00	1.47	0.57	1240	...	1.258	+0.090	-27.11
0052+251	87	30	9.0	20	10	0.34	0.10	0.23	2.48	5200	-.030	1.040	-0.062	-28.33
0157+001	79	47	11.0	56	14	0.59	0.14	0.71	2.08	2460	-.021	1.083	+0.003	-28.78
0804+761	119	9	2.5	80	5	0.08	0.02	0.67	0.46	3070	+.084	1.096	+0.028	-26.85
0838+770	102	13	14.9	91	30	0.13	0.15	0.89	0.65	2790	+.041	1.228	+0.102	-26.61
0844+349	76	8	10.5	68	10	0.10	0.14	0.89	0.55	2420	+.068	1.099	+0.059	-25.53
0921+525	145	83	28.9	20	20	0.58	0.20	0.14	2.52	2120	+.101	1.108	-0.084	-26.05
0923+129	76	31	17.7	40	13	0.41	0.23	0.53	1.47	1990	+.046	1.186	-0.031	-25.31
0923+201	159	7	0.0	114	16	0.04	0.00	0.72	0.60	7610	-.025	1.151	-0.033	-26.63
0934+013	92	51	29.3	44	22	0.55	0.32	0.48	1.89	1320	-.067	1.205	-0.084	-25.70
0947+396	110	15	18.7	25	15	0.13	0.17	0.23	1.22	4830	-.023	1.000	-0.148	-27.14
0953+414	156	18	8.6	39	13	0.12	0.06	0.25	0.84	3130	+.041	1.108	-0.035	-28.81
1001+054	89	7	7.0	73	20	0.08	0.08	0.82	0.23	1740	-.076	1.328	+0.082	-26.15
1004+130	43	6	0.0	10	10	0.15	0.00	0.23	1.60	6300	+.169	1.355	+0.065	-28.00
1011-040	45	15	10.2	33	16	0.34	0.22	0.73	1.11	1440	+.097	1.208	-0.026	-25.68
1012+008	104	29	6.3	69	15	0.28	0.06	0.66	1.00	2640	-.015	1.138	+0.049	-28.46
1022+519	69	7	19.2	74	12	0.11	0.28	1.08	0.50	1620	+.010	1.154	+0.038	-23.56
1048+342	230	28	32.0	73	50	0.12	0.14	0.32	1.83	3600	+.051	1.389	+0.045	-27.62
1048-090	81	28	6.4	0	15	0.34	0.08	0.09	4.45	5620	+.069	1.218	-0.224	-29.44
1049-006	106	55	10.5	59	59	0.52	0.10	0.56	3.92	5360	-.051	1.227	-0.044	-30.27
1100+772	90	41	4.1	19	19	0.46	0.05	0.21	3.99	6160	+.063	1.107	-0.097	-29.89
1103-006	79	8	6.0	47	25	0.11	0.08	0.60	0.88	6190	+.054	1.253	-0.152	-28.27
1114+445	100	17	3.6	20	15	0.17	0.04	0.20	1.36	4570	+.020	1.123	+0.080	-27.10
1115+407	61	6	0.0	33	16	0.10	0.00	0.54	0.41	1720	+.081	1.113	-0.025	-25.69
1116+215	175	10	3.5	81	6	0.06	0.02	0.47	0.34	2920	-.034	1.164	+0.025	-28.11
1119+120	49	19	9.4	44	6	0.38	0.19	0.90	1.42	1820	-.055	1.132	-0.010	-25.68
1121+422	89	5	17.8	33	16	0.06	0.20	0.37	2.55	2220	-.059	1.110	-0.078	-26.11
1126-041	102	19	7.3	109	11	0.19	0.07	1.07	0.93	2150	-.050	1.133	+0.017	-26.22
1149-110	118	33	33.9	43	12	0.28	0.29	0.36	1.78	3060	-.021	1.111	-0.131	-25.71
1151+117	128	11	1.7	31	16	0.09	0.01	0.24	1.00	4300	-.012	1.174	+0.076	-26.68
1202+281	143	36	8.6	41	20	0.25	0.06	0.29	2.27	5050	-.074	1.312	-0.298	-27.64
1211+143	84	12	13.2	44	10	0.14	0.16	0.52	0.55	1860	+.012	1.151	-0.003	-27.26
1216+069	87	10	4.5	17	8	0.11	0.05	0.20	1.19	5190	+.033	1.144	+0.046	-28.81
1226+023	113	5	3.4	64	6	0.04	0.03	0.57	0.33	3520	+.038	1.142	+0.044	-28.85
1229+204	106	19	14.5	63	7	0.18	0.14	0.59	1.46	3360	+.005	1.158	+0.022	-26.25
1244+026	41	17	21.3	50	15	0.41	0.51	1.20	1.00	830	+.154	1.247	+0.112	-24.86
1259+593	61	0	0.0	81	16	0.00	0.00	1.27	0.00	3390	...	1.107	+0.109	-26.07
1302-102	28	9	0.0	17	10	0.33	0.00	0.60	1.36	3400	+.027	1.021	-0.024	-29.02
1307+085	128	32	6.5	24	12	0.25	0.05	0.19	2.26	2360	-.065	1.068	-0.089	-28.31

122

TABLE 2—Continued

PG QSO (1)	EW Hβ (2)	EW λ5007 (3)	EW λ4686 (4)	EW Fe II (5)	σ_FeII (6)	R λ5007 (7)	R λ4686 (8)	R Fe II (9)	Peak λ5007 (10)	Hβ FWHM (11)	Hβ shift (12)	Hβ shape (13)	Hβ asymm (14)	M_[OIII] (15)
1309+355	51	19	0.0	14	10	0.37	0.00	0.28	1.86	2940	+.064	1.158	-0.193	-27.96
1310-108	98	77	36.3	37	12	0.79	0.37	0.38	4.58	3630	-.080	1.099	-0.075	-26.07
1322+659	77	8	20.0	45	11	0.10	0.26	0.59	0.72	2790	-.025	1.181	-0.009	-26.45
1341+258	120	14	16.2	45	11	0.12	0.14	0.38	0.95	3040	-.045	1.099	-0.066	-25.58
1351+236	23	12	0.0	27	14	0.52	0.00	1.18	2.80	6540	-.007	1.210	+0.135	-25.09
1351+640	58	31	7.5	14	14	0.54	0.13	0.24	2.27	5660	+.024	0.950	+0.136	-27.82
1352+183	133	10	8.2	61	15	0.07	0.06	0.46	0.58	3600	+.023	1.072	-0.021	-26.62
1354+213	58	31	2.1	18	18	0.54	0.04	0.31	2.75	4140	-.087	1.285	-0.063	-28.08
1402+261	76	1	0.0	94	16	0.02	0.00	1.23	0.09	1910	...	1.102	+0.042	-24.85
1404+226	54	7	0.0	54	11	0.12.	0.00	1.01	0.18	880	+.145	1.347	+0.112	-24.98
1411+442	106	15	6.4	52	9	0.14	0.06	0.49	0.63	2670	-.107	1.189	-0.046	-26.45
1415+451	58	1	2.3	73	12	0.02	0.04	1.25	0.10	2620	+.157	1.095	+0.106	-23.30
1416-129	174	49	6.1	31	31	0.28	0.04	0.18	2.19	6110	+.016	1.313	-0.175	-28.78
1425+267	93	36	1.8	10	10	0.38	0.02	0.11	4.31	9410	+.052	1.204	-0.052	-30.06
1426+015	88	11	6.0	34	12	0.13	0.07	0.39	1.47	6820	-.072	1.012	+0.033	-26.70
1427+480	137	58	21.1	50	25	0.43	0.15	0.36	1.99	2540	+.090	1.120	-0.077	-28.46
1435-067	142	12	6.4	64	12	0.09	0.05	0.45	0.59	3180	-.028	1.126	+0.029	-26.84
1440+356	64	10	3.7	76	7	0.15	0.06	1.19	0.31	1450	-.091	1.124	-0.026	-25.95
1444+407	72	1	0.0	104	10	0.02	0.00	1.45	0.12	2480	...	1.137	+0.085	-25.55
1448+273	39	22	5.7	35	9	0.57	0.15	0.90	1.51	910	-.050	1.280	+0.041	-26.67
1501+106	139	64	20.5	48	24	0.46	0.15	0.35	3.92	5470	-.036	1.037	-0.039	-27.27
1512+370	122	57	9.0	0	30	0.46	0.07	0.00	4.00	6810	+.024	1.251	-0.041	-30.31
1519+226	105	4	5.8	106	20	0.03	0.06	1.01	0.16	2220	+.041	1.104	+0.095	-25.15
1534+580	97	79	39.1	26	20	0.81	0.40	0.27	5.31	5340	-.032	1.024	+0.044	-26.18
1535+547	109	16	22.6	51	12	0.15	0.21	0.47	0.55	1480	-.101	1.264	+0.021	-25.16
1543+489	80	0	0.0	69	17	0.00	0.00	0.86	0.00	1560	...	1.298	-0.166	-24.85
1545+210	96	33	1.8	0	19	0.34	0.02	0.00	3.66	7030	+.086	1.184	-0.095	-29.42
1552+085	46	3	2.1	47	12	0.06	0.05	1.02	0.22	1430	-.010	1.203	+0.069	-24.88
1612+261	176	157	22.0	31	20	0.89	0.12	0.18	4.46	2520	+.007	1.105	+0.064	-29.26
1613+658	110	20	2.5	42	14	0.18	0.02	0.38	1.99	8450	-.056	1.155	-0.207	-27.47
1617+175	115	7	5.1	69	14	0.07	0.04	0.60	0.48	5330	-.032	1.262	-0.111	-26.14
1626+554	143	9	11.8	46	11	0.06	0.08	0.32	0.56	4490	+.024	1.087	-0.132	-25.96
1700+518	55	0	0.0	78	8	0.00	0.00	1.42	0.00	2210	...	1.387	+0.249	-25.69
1704+608	28	27	0.0	0	14	0.94	0.00	0.00	6.50	6560	+.042	1.280	-0.288	-29.95
2112+059	120	0	0.0	75	15	0.00	0.00	0.63	0.00	3190	...	1.193	-0.019	-26.51
2130+099	109	20	11.2	70	15	0.18	0.10	0.64	0.89	2330	-.083	1.101	-0.109	-26.49
2209+184	115	15	0.0	50	25	0.13	0.00	0.44	1.67	6500	-.070	1.192	+0.051	-26.10
2214+139	107	9	3.5	34	17	0.08	0.03	0.32	0.87	4550	+.119	1.248	+0.164	-25.76
2233+134	67	12	3.6	60	15	0.17	0.05	0.89	0.77	1740	-.015	1.181	+0.071	-27.85
2251+113	82	19	2.3	26	13	0.23	0.03	0.32	1.69	4160	-.135	1.216	-0.083	-29.45
2304+042	98	27	13.6	9	9	0.27	0.14	0.09	2.64	10120	-.080	0.954	+0.050	-25.15
2308+098	90	17	2.7	0	32	0.19	0.03	0.00	2.27	7970	-.013	1.146	-0.189	-29.34

123

TABLE 3
LINE AND CONTINUUM CORRELATION MATRIX

	z	M$_V$	Log R	α_{ox}	EW Hβ	EW λ5007	EW λ4686	EW Fe II	R λ5007	R λ4686	R Fe II	Peak λ5007	Hβ FWHM	Hβ shift	Hβ shape	Hβ asymm	M$_{[OIII]}$
z		−0.871	0.252	0.238	−0.083	−0.180	−0.419	−0.128	−0.156	−0.442	−0.134	0.098	0.307	0.031	0.228	−0.171	−0.554
M$_V$	−0.871		−0.376	−0.229	0.053	0.289	0.588	0.050	0.267	0.612	0.098	0.025	−0.275	−0.076	−0.191	0.104	0.650
Log R	0.252	−0.376		−0.088	−0.145	0.200	−0.146	−0.404	0.292	−0.128	−0.319	0.364	0.303	0.237	0.052	−0.273	−0.540
α_{ox}	0.238	−0.229	−0.088		−0.318	−0.413	−0.358	0.132	−0.261	−0.301	0.209	−0.319	−0.086	0.165	0.328	0.225	0.075
EW Hβ	−0.083	0.053	−0.145	−0.318		0.363	0.324	0.142	−0.103	−0.010	−0.425	0.065	0.181	−0.149	−0.088	−0.185	−0.188
EW λ5007	−0.180	0.289	0.200	−0.413	0.363		0.488	−0.389	0.803	0.311	−0.462	0.716	0.136	−0.029	−0.197	−0.239	−0.345
EW λ4686	−0.419	0.588	−0.146	−0.358	0.324	0.488		−0.077	0.355	0.876	−0.222	0.271	−0.199	−0.120	−0.167	−0.119	0.165
EW Fe II	−0.128	0.050	−0.404	0.132	0.142	−0.389	−0.077		−0.529	−0.084	0.766	−0.670	−0.436	−0.155	0.122	0.454	0.494
R λ5007	−0.156	0.267	0.292	−0.261	−0.103	0.803	0.355	−0.529		0.347	−0.365	0.827	0.139	0.010	−0.113	−0.288	−0.361
R λ4686	−0.442	0.612	−0.128	−0.301	−0.010	0.311	0.876	−0.084	0.347		−0.042	0.181	−0.288	−0.053	−0.140	−0.039	0.270
R Fe II	−0.134	0.098	−0.319	0.209	−0.425	−0.462	−0.222	0.766	−0.365	−0.042		−0.635	−0.548	−0.001	0.198	0.591	0.604
Peak λ5007	0.098	0.025	0.364	−0.319	0.065	0.716	0.271	−0.670	0.827	0.181	−0.635		0.508	−0.003	−0.121	−0.472	−0.555
Hβ FWHM	0.307	−0.275	0.303	−0.086	0.181	0.136	−0.199	−0.436	0.139	−0.288	−0.548	0.508		−0.068	−0.146	−0.316	−0.450
Hβ shift	0.031	−0.076	0.237	0.165	−0.149	−0.029	−0.120	−0.155	0.010	−0.053	−0.001	−0.003	−0.068		0.130	0.119	−0.011
Hβ shape	0.228	−0.191	0.052	0.328	−0.088	−0.197	−0.167	0.122	−0.113	−0.140	0.198	−0.121	−0.146	0.130		0.066	−0.028
Hβ asymm	−0.171	0.104	−0.273	0.225	−0.185	−0.239	−0.119	0.454	−0.288	−0.039	0.591	−0.472	−0.316	0.119	0.066		0.481
M$_{[OIII]}$	−0.554	0.650	−0.540	0.075	−0.188	−0.345	0.165	0.494	−0.361	0.270	0.604	−0.555	−0.450	−0.011	−0.028	0.481	

TABLE 4

CORRELATIONS OF EIGENVECTORS WITH LINE AND CONTINUUM PROPERTIES

Property	Eigenvector 1 29.2%	Eigenvector 2 50.9%	Eigenvector 3 61.4%	Eigenvector 4 68.2%	Eigenvector 5 74.2%
M_V	−0.269	+0.852	−0.087	+0.098	+0.051
Log R	+0.566	−0.324	−0.404	−0.148	+0.182
α_{ox}	−0.340	−0.543	−0.242	+0.144	−0.220
EW Hβ	+0.265	+0.153	+0.715	+0.412	+0.314
R λ5007	+0.598	+0.452	−0.510	−0.002	−0.183
R λ4686	−0.033	+0.792	−0.253	+0.186	+0.027
R Fe II	−0.832	−0.078	−0.201	−0.166	−0.145
Peak λ5007	+0.845	+0.269	−0.270	−0.003	−0.125
Hβ FWHM	+0.654	−0.221	+0.235	−0.240	−0.023
Hβ shift	−0.025	−0.229	−0.504	+0.116	+0.773
Hβ shape	−0.173	−0.400	−0.288	+0.732	−0.220
Hβ asymm	−0.679	−0.067	−0.119	−0.233	+0.153
$M_{[O\ III]}$	−0.811	+0.400	+0.007	−0.061	+0.065

tion. The observations from which this number was calculated (Kellermann et al. 1989) were made at 5 GHz with 18″ resolution. We have chosen log R = 1 as a reasonable dividing line between radio-loud objects and radio-quiet (see Fig. 5 in Kellermann et al. 1989). This means that 17 of the 87 objects are radio-loud and 70 are radio-quiet. We have searched the literature for information about the spectral index and radio morphology of these 17 radio-loud sources, and have separated them into steep-spectrum (typically double lobed) sources and flat-spectrum (typically compact) sources. There are 12 of the former and five of the latter. Note that this sample is optically selected with no regard for radio properties. A comparison of the properties of the radio-loud objects with the radio-quiet objects is an unbiased comparison if the radio loudness does not influence either the optical luminosity or the UV excess. However, it is possible that steep and flat radio sources would

differ in their observed properties, so it is important to maintain this distinction throughout the discussion. Figures 2 and 3 show radio-quiet objects as solid squares, steep-spectrum radio sources as open circles, and flat-spectrum radio sources as open triangles.

It is seen clearly in Figures 2 and 3 that the radio sources are not mixed uniformly with the radio-quiet QSOs but tend toward the end having a large value of Peak λ5007 and small value of EW Fe II. Furthermore, the steep-spectrum sources are the most extreme of these, with the few flat-spectrum sources lying more towards the middle of the radio-quiet distribution. Figure 4 presents a histogram of the EW Fe II values shown separately for the steep, flat, and quiet objects. Note that the radio-quiet objects lie in a broadly peaked distribution
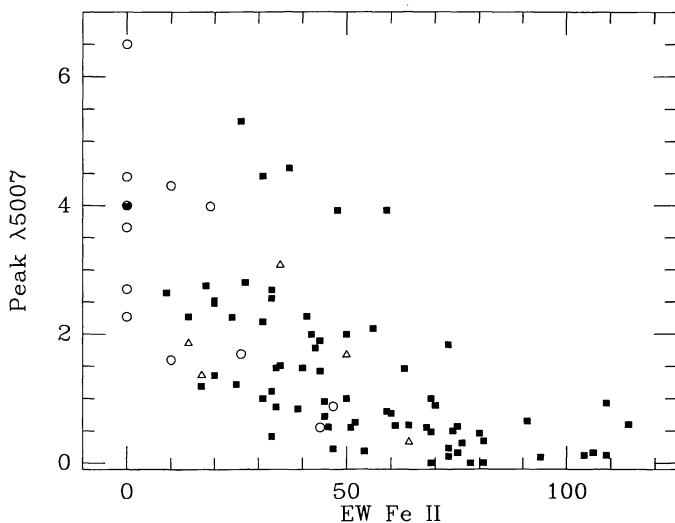
FIG. 2.—Ratio of peak height of [O III] λ5007 to that of Hβ plotted against equivalent width of the Fe II emission between λ4434 and λ4684. Solid squares are radio-quiet objects, open circles are steep-spectrum radio sources, and open triangles are flat-spectrum radio sources.
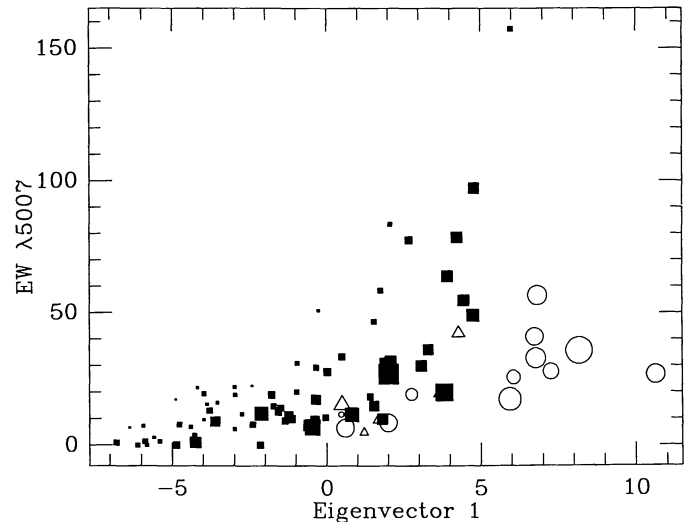

FIG. 3.—Equivalent width of [O III] λ5007 plotted against the projection on eigenvector 1. As in Fig. 2, solid squares represent radio-quiet objects, open circles are steep-spectrum radio sources, and open triangles are flat-spectrum radio sources. The size of each point is proportional to the FWHM of the Hβ line in that object. Note that at a given value of eigenvector 1, the points with larger EW λ5007 have narrower broad lines.
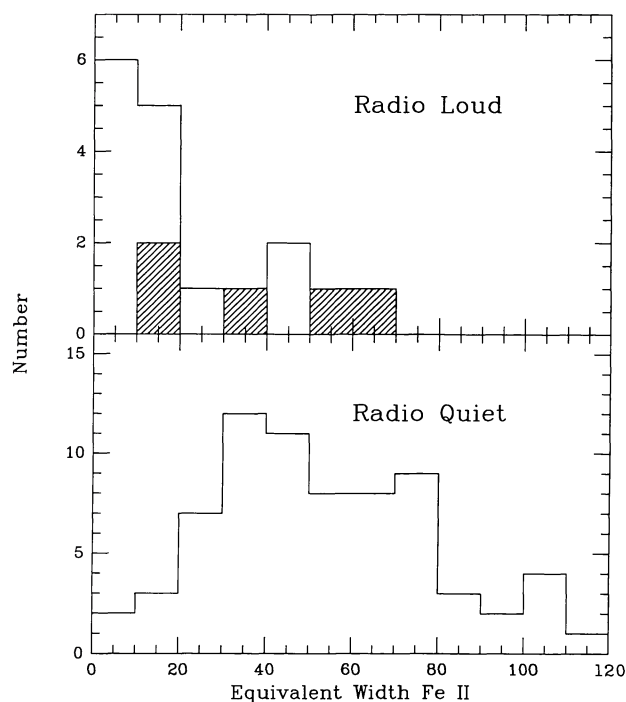
FIG. 4.—Histograms of the equivalent width of the Fe II emission between $\lambda 4434$ and $\lambda 4684$ for 17 radio-loud QSOs (*top panel*) and 70 radio-quiet QSOs (*bottom panel*). In the top panel, shaded areas represent flat-spectrum radio sources and unshaded areas represent steep-spectrum radio sources.

extending from 0 to 120 Å equivalent width. The steep spectrum sources almost all lie below 20 Å equivalent width while the flat spectrum sources sparsely cover the range of the peak in the radio quiet distribution. This result is identical to that found by Joly (1991) who compiled Fe II measurements of almost 200 objects from the literature, concentrating on radio-loud QSOs. A statistical treatment of these differences is given in § 4.

In addition to log R, the other two properties which are correlated with the first eigenvector are Hβ FWHM and Hβ asymmetry. It is well known that steep-spectrum (lobe-dominated) radio sources tend to have broader permitted lines than do flat-spectrum (core-dominated) radio sources (Setti & Woltjer 1977; Miley & Miller 1979; Boroson & Oke 1984; Wills & Browne 1986). In the unification scheme of Orr & Browne (1982), this is attributed to a viewing angle effect in which most of the motion of the BLR clouds is constrained to a disk perpendicular to the axis of the radio jet. In this sample, it can be seen that the line width effects persist in the radio-quiet objects. Table 3 shows that objects with strong Fe II and weak [O III] tend to have narrow lines and objects with weak Fe II and strong [O III], predominantly steep-spectrum radio-loud QSOs, have broader lines. A correlation analysis of the radio-quiet objects only confirms that these correlations are not limited to the radio-loud objects.

The Hβ asymmetry index is also connected with the Fe II–[O III] anticorrelation. The index we have calculated was defined and measured for a small sample of objects by De Robertis (1985) who calls it α_β. A more comprehensive study of line asymmetries has been made by Sulentic (1989) who compiled

a total of 61 Hβ profiles from the literature (27 from De Robertis 1985) and measured the same index. Both of these authors reached the same conclusion: a large fraction of profiles are asymmetric and both blue and red asymmetries are seen. Neither of these studies found any systematic relation between the direction or size of the asymmetry and any other property. Corbin (1991) has compared spectra of 45 steep and flat radio spectrum QSOs with $z \sim 2$. He finds that the steep-spectrum objects tend to have red asymmetric C IV $\lambda 1549$ profiles and that the flat-spectrum objects have blue asymmetric profiles. Figure 5 is a plot of Hβ asymmetry against EW Fe II. Rather than a linear relation, the plot gives the impression that there is a broad range of asymmetries seen at small R Fe II values though most are negative (red), but at large R Fe II values only positive (blue) asymmetries are seen. This correlation is shown in a different way in Figure 6 which displays the Hβ profile in a number of objects with the largest blue and red asymmetries. The difference in [O III] strength between the two groups is striking; the red asymmetric profiles occur in objects which have quite strong [O III], while in the blue asymmetric objects [O III] is extremely weak or absent entirely. Note also that the profiles become more and more asymmetric at lower flux levels. Had line centroids at $\frac{1}{10}$ maximum been used instead of $\frac{1}{4}$ maximum, the values of the asymmetries would have been much larger.

3.2. Eigenvector 2: the Luminosity Dependence of He II $\lambda 4686$

Eigenvector 2 is dominated by the inverse correlation between the strength of He II $\lambda 4686$ and optical luminosity. This correlation has been noted by Heckman (1980) based on a small number of QSOs, but it is obvious from many of the spectra shown in Figure 1 that reliable estimates of the $\lambda 4686$ strength require an accurate subtraction of Fe II. The relation between R $\lambda 4686$ and M_v ($r = 0.650$) is shown in Figure 7. Also associated with eigenvector 2 is α_{ox}, although the correlation is weaker. The definition of α_{ox} is such that larger values indicate weaker X-ray flux relative to optical flux.
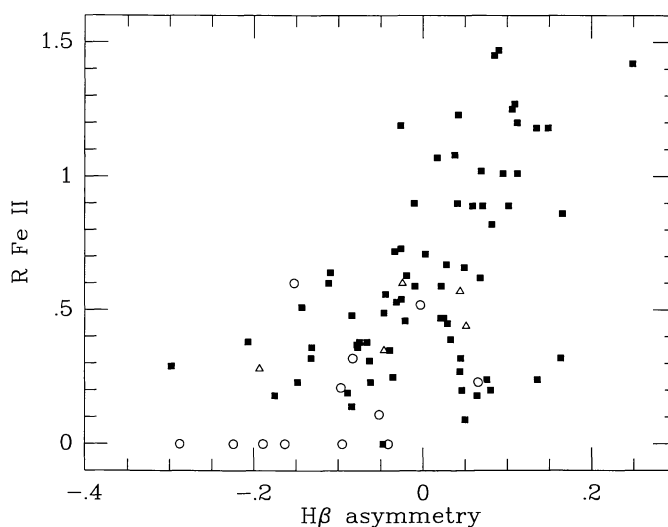

FIG. 5.—Ratio of the equivalent width of Fe II to that of Hβ plotted against the Hβ asymmetry index. The asymmetry index (in units of the FWHM of the line) is defined such that a positive index indicates excess emission on the blue wing. Symbols are as in Fig. 2.
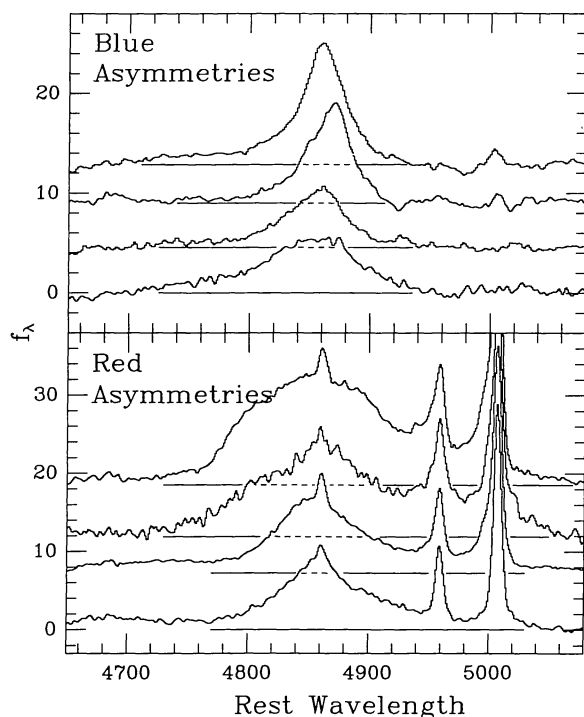
FIG. 6.—Examples of profile asymmetries in Hβ. Plotted are Fe II subtracted and continuum-subtracted spectra in f_λ units with arbitrary scaling and offsets against rest wavelength. Zero level of each spectrum is indicated. From top to bottom objects are (*top panel*) PG 1444+407, PG 1415+451, PG 1259+593, PG 0043+039, and (*bottom panel*) PG 1613+658, PG 2308+098, PG 1202+281, PG 0003+158. Note the difference in [O III] λλ4959, 5007 between the blue asymmetric and red asymmetric profiles.

3.3. The Remaining Eigenvectors

It can be seen in Table 4 that each of the next three eigenvectors is dominated by a single property, EW Hβ, Hβ shape, and Hβ shift, respectively. Table 3 indicates that these properties have few correlations with other properties. EW Hβ shows modest correlations with EW λ5007 and EW λ4686 and anticorrelations with α_{ox} and R Fe II. Hβ shape is anticorrelated with α_{ox}, and Hβ shift is not significantly correlated with any of the other properties. The fact that these eigenvectors together account for 23% of the variance in the measured properties suggests that there is real scatter in their values and that they are driven by different physical parameters than are the first two eigenvectors.

4. DISCUSSION

In this section we examine the implications of the analysis described above. Of paramount interest is the connection between the observed properties and the physical parameters of the objects. We begin by discussing the eigenvectors and their relation to the physical mechanisms.

4.1. Interpretation of the Eigenvectors

Can the eigenvectors be associated with individual physical parameters, or are they more complex, representing combinations of physical properties which themselves vary together? In

what might be called the standard model of a QSO, there are several obvious parameters which are expected to influence the observed properties. These are (1) the accretion rate, (2) the mass of the accreting object, M_{BH}, or equivalently, the ratio of the accretion rate to the Eddington rate, (3) the covering factor of the BLR clouds (which might be related to both a geometrical factor and an optical depth), (4) the degree of anisotropy in the pattern of emitted radiation from the continuum source, (5) the orientation of the axis of the accretion and/or outflow to the line of sight, (6) the velocity distribution of the BLR clouds, (7) the ionization parameter, and (8) the anisotropy of the radiation emitted from the BLR cloud. Clearly some of these are expected to be correlated. For example, the greater the degree of anisotropy, the larger the effects due to orientation.

The first eigenvector is dominated by the anticorrelation between the Fe II strength and the [O III] λ5007 strength. One might suppose that this has something to do with the amount of ionizing radiation that gets out into the narrow-line region—in some objects little energy goes into pumping Fe II in the BLR either because of a small geometric cross section for the relevant clouds (covering factor) or because they have little optical depth at the relevant frequencies. In these objects the narrow lines are strong. In other objects the reverse is true. This interpretation is complicated, however, by the fact that our measurements all reference the Fe II and [O III] line strength to something else, either the continuum or the Hβ strength. It is possible that other effects may conspire to produce this apparent correlation. Such an explanation is argued by the proponents of strong beaming and orientation effects.

Blandford & Rees (1978) first proposed that orientation effects were important in understanding the observed properties of QSOs particularly at radio frequencies. Since bulk relativistic motion is implied by the discovery of superluminal motion in a substantial number of objects, doppler boosting of the core, possibly even at optical frequencies, is expected. Scheuer & Readhead (1979) used this concept to develop a model in which the degree of radio loudness (and its morphology) is a
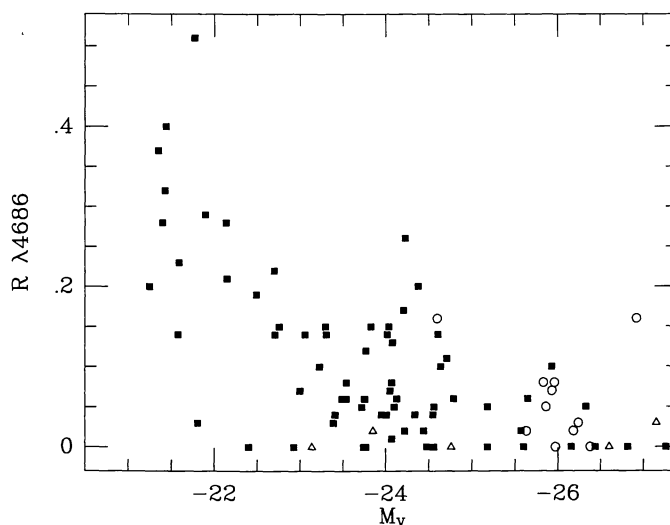

FIG. 7.—Ratio of the equivalent width of He II λ4686 plotted against the absolute v magnitude. Symbols are as in Fig. 2.

function of the orientation of the radio jet to the line of sight. They argued that radio-quiet QSOs could be explained as objects in which the jet was close to the plane of the sky. Based on difficulties with the radio luminosity distribution and the evidence for extended radio emission even in core-dominated radio-loud QSOs, Orr & Browne (1982) removed the radio-quiet QSOs from the picture and proposed a model in which all radio-loud QSOs were the same type of object with orientation determining the morphology of the radio emission. This idea was further extended by Barthel (1989) who argued that radio galaxies should be included as the objects with radio axes closest to the plane of the sky.

While it is undoubtedly true that the radio and optical structures in at least some QSOs are not spherically symmetric, there is little hard evidence that orientation effects dominate the optical properties of QSOs. Despite this, several studies have attempted to interpret correlations among observed properties in terms of the beaming model—generally by requiring that lines and continuum are emitted anisotropically, due either to relativistic effects in the case of the continuum or to a flattened geometry for the emitting region. Miley & Miller (1979) showed that lobe-dominated QSOs have broader permitted lines than do core-dominated QSOs. Wills & Browne (1986) quantified this effect by studying the relation between FWHM of Hβ and R, the ratio of core to lobe radio flux. They found an upper envelope on the FWHM distribution which extended to larger FWHM at smaller values of R (lobe-dominated sources). They interpreted this as consistent with the beaming model if the gas motions are confined to a disk perpendicular to the radio jet axis. Browne & Wright (1985) argue that a 1 mag difference in the magnitude distributions of core- and lobe-dominated radio-loud QSOs implies that the optical continuum in core-dominated objects is enhanced by this factor. Jackson & Browne (1991) have measured Fe II and Hβ in samples of lobe-dominated and core-dominated QSOs and conclude that both of these lines are also emitted anisotropically but to differing degrees. The fact that Fe II, [O III], and Hβ FWHM appear to separate the core-dominated and lobe-dominated QSOs suggests that eigenvector 1 may be correlated with the orientation of the preferred axis of the object with respect to the line of sight.

With two caveats, the data set presented in this paper are relevant to the beaming model and orientation effects in general. Because radio properties played no role in the selection of these objects, any argument about matching *radio* properties of samples to be compared does not apply. However, the currently preferred beaming model refers only to radio sources. Thus, we must either decide that the same physical processes are responsible for the observable emission-line properties in radio-loud and radio-quiet objects or that they are intrinsically different types of objects, and anything one learns from radio-quiet QSOs is inapplicable to radio-loud QSOs. Of course, there is a middle ground, which represents the reasonable view that the radio-loud–radio-quiet distinction may be a manifestation of the same physical processes which govern the observed properties; i.e., perhaps the covering factor of the BLR is different in the two types of object, yielding different orientation effects. The second concern is the proposed enhancement of the optical continuum due to orientation (Browne & Wright 1985). If flat-spectrum objects appear 1

mag brighter than their "isotropic" luminosity, any measured property correlated with absolute magnitude will be shifted by some amount to values corresponding to lower luminosities.

With that in mind, we show in Figure 8 a plot of the [O III] absolute magnitude, $M_{[O\ III]}$, versus eigenvector 1. An extremely good correlation ($r = -0.811$ from Table 4) is obvious. It has been argued that $M_{[O\ III]}$ should be orientation independent since it arises from the large and optically thin narrow-line region (Jackson et al. 1989). If eigenvector 1 is highly correlated with an isotropic property, it must not itself represent a primarily anisotropic property. Now we must consider the possible effect of orientation on optical luminosity. Suppose eigenvector 1 were mostly dependent upon orientation such that the strong Fe II–weak [O III] objects were being seen pole-on and the weak Fe II–strong [O III] objects were being seen edge-on, as the beaming model would indicate. In that case, the weak [O III] objects have weak [O III] relative to the continuum *because the continuum has been enhanced due to the orientation of the object.* Suppose, in addition, that there is a relation between absolute magnitude and $M_{[O\ III]}$ such that objects with higher overall luminosity have higher [O III] luminosity. Then the "isotropic" overall luminosity of the pole-on objects would be considerably lower than the measured M_v, and they would be expected to have lower [O III] luminosity. This effect would explain the correlation seen in Figure 8. However, if this were true, M_v and $M_{[O\ III]}$ would be strongly anti-correlated because the objects with the lowest luminosity [O III] emission would be those with the most enhanced optical continuum. Table 3 shows that this is not the case, $M_{[O\ III]}$ and M_v are highly correlated ($r = 0.650$). In fact, the steep-spectrum objects have both the greatest continuum luminosity and the greatest [O III] luminosity, so this selection effect cannot, in general, be responsible for the excellent correlation between eigenvector 1 and $M_{[O\ III]}$.
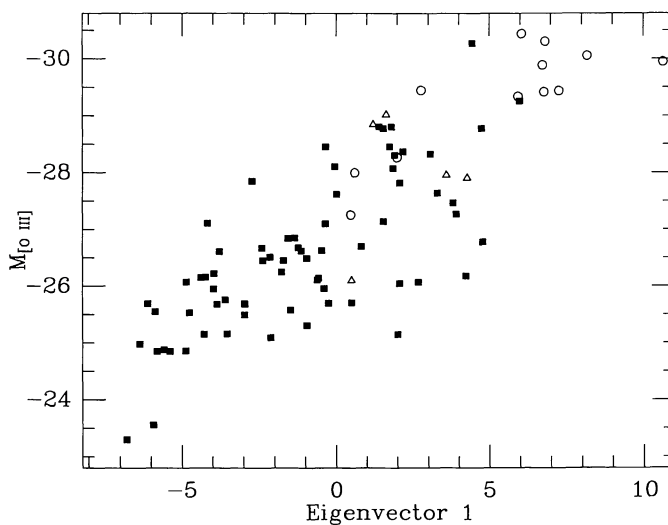
Although we rule out the standard beaming model as pro-

FIG. 8.—Monochromatic absolute magnitude in the [O III] λ5007 line plotted against the projection of each object along eigenvector 1, the vector accounting for the largest fraction of the variance within the sample. The units in which the eigenvector is plotted are arbitrary. Symbols are as in Fig. 2.

viding the explanation for most of the variance in the sample, we cannot rule out geometric effects *intrinsic* to the QSO, and, in fact, we believe that there is much evidence to support the existence of these. For example, a model in which the broad-line clouds form a toroidal distribution which is capable of preventing ionizing radiation from getting out to a planar narrow-line region may qualitatively explain most of the correlations which define eigenvector 1. The Fe II could be dependent on the cross-section such a torus presents to the continuum source, while Hβ, optically thick, is emitted at the surface, the area of which changes only slightly as the torus thickens. That is, the optically thin Fe II is more proportional to the volume of the BLR while Hβ depends more on the surface area. If this is correct, eigenvector 1 is driven by an increase in covering factor as one moves from the radio-loud objects at the strong [O III], weak Fe II end of the sequence to the weak [O III], strong Fe II objects at the other end. This sort of behavior is thought to be dependent on the ratio of the accretion rate to the Eddington rate—governed at a particular accretion rate by the mass of the black hole. Interestingly, one of the most extreme objects at the "high covering factor" end is the low-ionization BAL QSO PG 1700+518. This explanation also qualitatively provides a mechanism for the FWHM effect seen in Figure 3. It may be that in the objects with stronger [O III] (at a given value of eigenvector 1), there is less material at small radii. If the vertical height of the disk is the same, these objects will have a smaller covering factor, allowing more radiation out to an ionization bounded narrow-line region. It is also notable that the FWHM correlation goes in the opposite sense than what would be predicted by the beaming model. In that model objects with narrow lines are those in which the continuum is being enhanced; they would then be expected to have smaller [O III] equivalent widths, not larger as is observed.

An additional argument can be made that the factor controlling the Fe II strength is geometric in nature rather than related to the spectral shape of the ionizing continuum. In most models, Fe II emission is produced in the extended warm region heated by soft X-rays. If the Fe II strength were enhanced in objects emitting more of these soft X-rays an anticorrelation between EW Fe II and α_{ox} would be expected. In fact, they show a weak correlation but at a level which is probably not significant.

An additional variable associated with eigenvector 1 is the Hβ asymmetry parameter which, as described in § 3, shows the trend that strong [O III]–weak Fe II objects tend to have red asymmetries while strong Fe II–weak [O III] objects tend to have blue asymmetries. Possible explanations for this correlation are discussed in § 4.3 below.

The second eigenvector is dominated by the luminosity of the object, and, in the standard model, this is determined by the accretion rate. The correlation with He II $\lambda4686$ is apparent in the literature on line strengths in Seyfert 1 galaxies and QSOs, although the only published statement on the subject is in Heckman's (1980) study of a small, heterogeneously selected sample of objects. As pointed out in that study, the most obvious explanation of this effect is that it depends on the hardness of the ionizing spectrum, and that lower luminosity objects have a larger number of ionizing photons below $\lambda228$ relative to $\lambda912$ than do higher luminosity objects. A similar conclusion, a decrease in ionization parameter at high energies

with luminosity, was drawn by Mushotzky & Ferland (1984) in a study aimed at understanding the cause for the "Baldwin effect" in terms of photoionization models. In support of this explanation we note the behavior of α_{ox} which ought to be sensitive to the spectral slope in that region. If hardness of the UV continuum is the cause of the change in the strength of $\lambda4686$, it is expected that α_{ox} would be smaller in objects with stronger He II and lower luminosity. Table 3 shows that this is just the case, with a correlation coefficient of -0.301 between α_{ox} and R $\lambda4686$.

Baldwin et al. (1989) investigated the relation between luminosity and the strengths of various lines for samples of radio and optically selected QSOs. They found that the ratio He II $\lambda1640$/C IV $\lambda1549$ is anticorrelated with absolute magnitude, unlike any of the other lines that they measured. This could be an analogous relation for the UV He II line. If a simple relation exists between the two He II lines, the two anticorrelations with absolute magnitude might provide a method of calculating the luminosities of high-redshift QSOs from a calibration at low redshift. In theory, this could be used to determine q_0.

The third, fourth, and fifth eigenvectors depend primarily on single properties, EW Hβ, Hβ shape, and Hβ shift. As stated above, these are not highly correlated with other properties, but there is no doubt that they account for a significant fraction of the variance in the sample. One can imagine that they represent physical properties that vary from object to object but do not interact with the physical mechanism itself in any major way. It is difficult to think of such properties, particularly in the case of EW Hβ, which one would assume would be governed by the optical depth of the clouds and the large-scale distribution of material, two things which we have argued are affecting other measurements.

4.2. The Differences among QSOs with Different Radio Properties

A somewhat different type of analysis is useful for comparing the properties of radio-quiet, steep-spectrum, and flat-spectrum objects. Rather than considering the trends in properties within the sample as a whole, we divide the sample into a number of subsamples and ask whether the distribution of a given property is different between two subsamples. In order to do this, we consider radio-quiet ($\log R < 1$, 70 objects), radio-loud ($\log R > 1$, 17 objects), steep-spectrum ($\log R > 1$ and $\alpha_{2,6} > 0.5$, 12 objects), flat-spectrum ($\log R > 1$ and $\alpha_{2,6} < 0.5$, five objects), and luminous radio-quiet ($\log R < 1$ and $M_v < -24.6$, 15 objects). We include this last category because the steep-spectrum radio-loud objects are found only among the more luminous objects in the sample and this constraint produces a reasonable match in the absolute magnitude distributions of radio-loud and radio-quiet subsamples. For each of 16 properties listed in Tables 1 or 2, we have used the Kolmogorov-Smirnov two sample test to determine the probability that the distribution of values in two subsamples is consistent with having been chosen from the same parent distribution. The columns in Table 5 list these probabilities, showing comparisons between radio-loud and radio-quiet, steep-spectrum and flat-spectrum, steep-spectrum and radio-quiet, flat-spectrum and radio-quiet, and steep-spectrum and luminous radio-quiet QSOs.

TABLE 5

K-S Probabilities that Samples with Different Radio Properties
Are Drawn from Same Distribution

Property	L vs. Q	S vs. F	S vs. Q	F vs. Q	S vs. Q $(M_V < -24.6)$
z	<0.001	0.038	<0.001	0.695	0.516
M_V	<0.001	0.303	<0.001	0.358	0.134
α_{ox}	0.778	0.677	0.772	0.882	0.658
EW Hβ	0.185	0.303	0.034	0.795	0.799
EW λ5007	0.608	0.426	0.289	0.992	<0.001
EW λ4686	0.031	0.118	0.343	0.012	0.002
EW Fe II	<0.001	0.087	<0.001	0.643	0.005
R λ5007	0.142	0.871	0.091	0.795	0.057
R λ4686	0.031	0.181	0.415	0.009	0.861
R Fe II	0.013	0.038	<0.001	0.358	0.016
Peak λ5007 ...	0.011	0.341	0.011	0.491	0.028
Hβ FWHM ...	0.001	0.236	<0.001	0.147	0.001
Hβ shift	0.011	0.677	0.052	0.221	0.010
Hβ shape	0.114	0.181	0.057	0.643	0.516
Hβ asymm	0.022	0.236	0.006	0.746	0.010
$M_{[O III]}$	<0.001	0.038	<0.001	0.059	0.004

Notes.—L = radio-loud, Q = radio-quiet, S = steep-spectrum, F = flat-spectrum.

Table 5 shows that there are quite significant differences among almost all the subsamples we have defined. The most dramatic distinctions occur in the comparison of radio-loud and radio-quiet for which 11 of the 16 properties show differences at better than the 95% confidence level. Various hypotheses about the nature of radio-loud and radio-quiet objects and the possibility that flat-spectrum and steep-spectrum sources are the same objects seen from different orientations can be tested with these comparisons. Suppose radio-loud and radio-quiet QSOs only differed in that the objects in one group have radio emission and the objects in the other group do not. Then the distribution over orientation ought to be the same for each subsample, and if the mix of flat spectrum and steep-spectrum radio-loud objects represents a distribution over orientation together with a selection effect having to do with the enhancement of brightness due to orientation, the radio-quiet objects should represent the same mix. That this idea is false can be easily seen from the comparison of radio-loud and radio-quiet subsamples. While flat-spectrum objects and radio-quiet objects have similar properties, steep-spectrum objects, which dominate the radio-loud subsample, are quite different. *There are no (or not many) radio-quiet analogs of the steep-spectrum radio QSOs.* Even if one considers only the high luminosity radio-quiet objects, the steep-spectrum radio sources are easily distinguishable on the basis of Fe II, Hβ profile parameters, and [O III] absolute magnitude. This suggests that radio loudness is tied to the physical parameters that drive eigenvector 1; objects with strong [O III] and weak Fe II are radio-loud while objects with strong Fe II and weak [O III] are radio-quiet.

Because there are only five flat-spectrum sources, less strong statements can be made about how they differ from the steep-spectrum objects. The property showing the greatest difference for any comparison involving the flat-spectrum objects is with the radio-quiet objects in the strength of He II λ4686. This can be seen in Figure 7 as well, where the flat-spectrum objects fall at the bottom of the envelope of objects. In fact, only two of the five flat-spectrum sources have λ4686 detected. It is likely,

however, that this difference is due to the correlation between λ4686 and absolute magnitude. While the flat-spectrum sources are not limited to the highest luminosity as are the steep-spectrum sources, Figure 7 shows that the radio-quiet objects which have very strong λ4686 emission all occur at $M_v > -23$, fainter than the faintest flat-spectrum object. The differences between the flat- and steep-spectrum QSOs are less significant, though differences at a significance level greater than 95% are seen in R Fe II and the isotropic property, $M_{[O III]}$.

It is interesting to note that the steep-spectrum QSOs are quite different in many properties from any of the other objects. Steep-spectrum objects have weaker Fe II and stronger [O III] than any other type—even in samples matched in luminosity. In many of the line profile parameters, also, the steep-spectrum objects are easily discerned from the radio-quiet QSOs. This suggests two possible interpretations. Either the steep-spectrum objects are the most extreme objects in relations defined by the radio-quiet objects, or they truly have discrepant properties, and these are responsible for giving the appearance of correlations in the sample as a whole. This question represents a more fundamental uncertainty about the nature of the physical properties which drive the appearance of the spectra. If the radio sources fall naturally on the relations defined by the radio-quiet subsample, and these relations also separate the flat- and steep-spectrum objects, that is a strong argument that the same physical properties, i.e., *not orientation,* differentiate the two different radio morphologies. If the radio sources, or even just the steep-spectrum objects, do not lie on the relations defined by the radio-quiet objects (or in the extreme case, if there are no relations defined by the radio-quiet objects), that is a strong argument that radio-loud and radio-quiet objects are entirely different things, and different physical properties may very well affect the properties of the two subsamples.

In all cases but one, it appears that the steep-spectrum sources are not discrepant objects but are, in fact, the tail of the relation defined by the radio-quiet objects. This can be seen in

Figure 2, which shows the Fe II–[O III] anticorrelation (Peak λ5007 vs. EW Fe II), and Figure 9, in which is plotted Hβ FWHM against R Fe II. In both of these cases, note that the solid points do show a correlation, and that the flat spectrum sources are mixed in with these but the steep spectrum sources fall along the logical extension of this relation. Similar behavior is seen in Figure 8 in which $M_{[O\ III]}$ is plotted against eigenvector 1. This strongly suggests that (1) radio-loud QSOs are not a physically distinct population of QSOs but represent the extreme of some physical property or properties which cause (or are a result of) their radio loudness as well as other observables, and (2) orientation effects are not the dominant factor in determining the observable properties of radio-loud objects.

The one new correlation apparent in Table 5 is that in terms of Hβ shift, the steep-spectrum QSOs are discernible. Table 3 shows that within the whole sample, Hβ shift is not strongly correlated with any property, although it is marginally correlated ($r = 0.237$) with log R. Figure 10 shows Hβ asymmetry plotted against Hβ shift. Recall that the uncertainty in the shift values is about 0.01, so almost all the shifts are significant. Although all four quadrants of this diagram are well populated, it is apparent that the radio-loud objects are predominantly found in the lower right quadrant—signifying red asymmetries and blueshifts. An idea of the significance of this effect can be obtained by asking what is the probability of finding 11 out of 17 of the radio-loud QSOs in one quadrant if the four quadrants had intrinsically equal likelihoods of being populated. The 11 objects then represent a 3.8 σ effect with a likelihood of 1.45×10^{-4}. The radio-quiet QSOs show a slight deficit (11/63) in the quadrant overpopulated by the radio-loud objects, but this is not statistically significant.

4.3. The Nature of Profile Asymmetries and Shifts

One of the most intriguing aspects of the line profiles in AGNs is the fact that they show asymmetries and shifts. These have been measured in a number of studies (Gaskell 1982; De
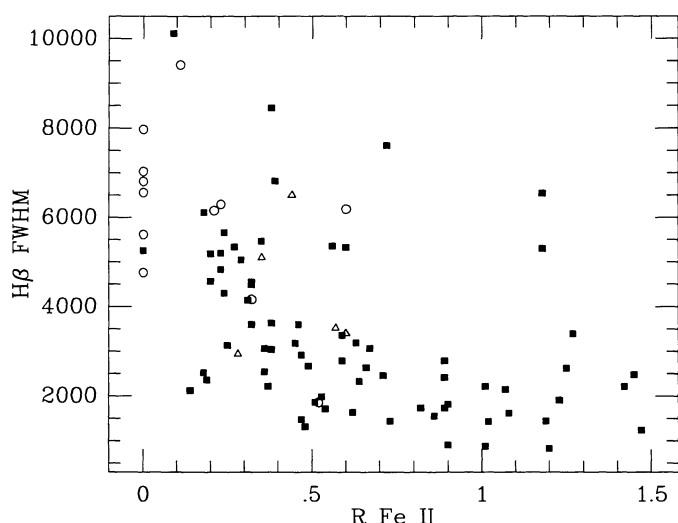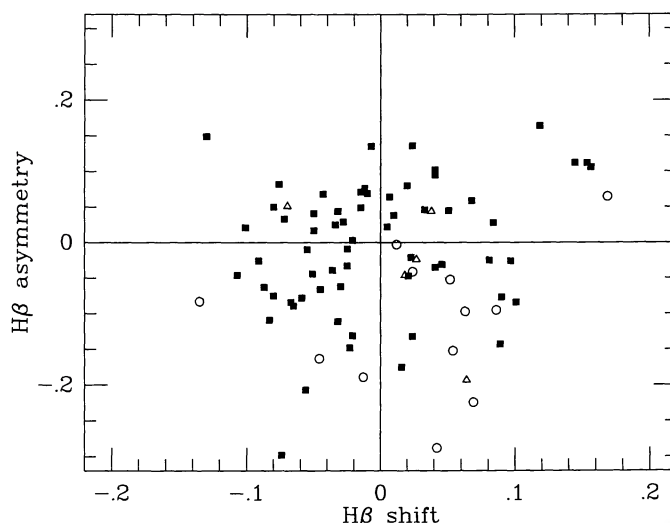
FIG. 10.—The Hβ asymmetry parameter plotted against the Hβ shift parameter. Both measurements are referenced to the FWHM of the Hβ line. The asymmetry parameter is defined such that a positive value indicates an excess on the blue side of the line and a negative value indicates an excess on the red side of the line. A positive value for the shift parameter indicates that the peak of the broad component is redward of the position expected on the basis of the forbidden lines. Symbols are as in Fig. 2. Note the excess of radio-loud objects in the lower right quadrant.

Robertis 1985; Jackson & Browne 1989; Sulentic 1989; Espey et al. 1989; Corbin 1990). Both redshifts and blueshifts and asymmetries are seen, although Jackson & Browne (1989) find only redshifts in their study of radio-loud QSOs. As has been pointed out by many of these authors, the measurement of the optical lines is complicated by the poorly known effects of contamination by weaker lines, particularly those of Fe II.

In this paper we report two newly discovered correlations involving the redshift of the peak and the asymmetry of the profile of the Hβ line. First, we find that radio-loud objects have Hβ lines which tend to be shifted to the red, while radio-quiet objects show equal shifts to the red and blue. Second, we see a correlation between the direction of the asymmetry and the group of properties which make up the largest fraction of the variance in the sample, including Fe II strength and [O III] strength (and also separating steep-spectrum radio sources from the flat-spectrum and radio-quiet objects). This correlation goes in the sense that strong Fe II–weak [O III] objects tend to have blue asymmetries and weak Fe II–strong [O III] objects tend to have red asymmetries. This also, of course, implies red asymmetries in steep-spectrum radio-loud QSOs, as found by Jackson & Browne (1989).

Before considering the implications of these trends for geometric and kinematic models, it is important to note the systematic effects which may influence the measurement of these quantities. For the objects in which Fe II emission is very strong, improper subtraction of that is certainly a concern. For example, one might worry that in removing the Hβ line from the spectrum of I Zw 1 in order to make the Fe II template, some Fe II lines blended with Hβ were inadvertantly removed also. If we consider the objects with very strong blue asymmetries, such as PG 0043+039, PG 1444+407, and PG 1259+593, the excess flux on the blue wing almost appears to

FIG. 9.—FWHM of the Hβ line plotted against R Fe II, the ratio of the equivalent width of the Fe II complex between λ4434 and λ4684 to that of Hβ.

be a distinct lump. In PG 1444+407, this lump is visible in the range $\lambda\lambda4650-4790$. In I Zw 1, there are several Fe II features in this range, including multiplet 43 which has lines at $\lambda4731.4$ and $\lambda4657.0$. Both of these are clearly visible in the original spectrum of I Zw 1 but were effectively removed by the Fe II subtraction process. In fact the residual emission in I Zw 1 in the range $\lambda\lambda4650-4790$ is only 4% of the Fe II flux in the measured range $\lambda\lambda4434-4684$, and some of this must be Hβ emission. In PG 1444+407 the flux in the lump on the blue side of Hβ is almost 10% of the strength of the subtracted Fe II. Thus, we think it unlikely that unsubtracted Fe II accounts for much of the blue wing of Hβ. Another way in which Fe II errors could produce this effect is if it were oversubtracted on the red wing of Hβ. This is a particular worry because of the evidence that multiplet 42 is one of the more discrepant features; however, we see no cases in which it is obviously weaker relative to the other Fe II lines than in our template, and so we believe that a substantial oversubtraction is unlikely.

A second concern is the possibility of broad [O III] producing a red wing on Hβ in the objects with strong [O III] emission. The possibility of a broad component of [O III] has been studied by Meyers & Peterson (1985) and van Groningen (1984) in a number of objects. These authors both claimed to find evidence of broad $\lambda5007$ emission, particularly on the red side of the line. However, Meyers & Peterson (1985) assumed the symmetry of the Hβ line, and van Groningen (1984) found that the existence of the red wing was very sensitive to the strength assumed for Fe II $\lambda5018$. The fact that the Fe II multiplet which seems to vary the most relative to the others is multiplet 42 which contaminates the red wing of Hβ suggests that a better approach would be to look carefully at the shape of Hα to try to separate a red wing on Hβ from broad [O III] emission.

If the line asymmetries are not due to contamination by other features but are real, they are caused by systematic motion of the broad-line emitting clouds combined with preferential viewing of different parts of the BLR. For example, a blue wing could be caused by outflowing clouds in which the far side is partially shielded from sight or infalling clouds in which the emission arises predominantly from the sides of the clouds facing the central continuum source. Alternatively, if the motion is rotational, relativistic effects can enhance the flux from the approaching material over that of the receding material producing an excess on the blue wing. We discuss this last possibility first. As has been pointed out by Sulentic et al. (1990), such relativistic accretion disks as the models of Chen, Halpern, & Filippenko (1989) and Dumont & Collin-Souffrin (1990) predict well-defined relations between measures of the asymmetry and the shift of the line centroid because both are effects of the same process. Sulentic et al. (1990) demonstrate the incompatibility of such models with existing measurements by plotting the asymmetry index (the same as the one given in this paper) against the Hβ profile centroid at various fractions of maximum. This profile centroid at $\frac{3}{4}$ maximum is similar to the Hβ shift parameter but is plotted as a wavelength rather than a shift in units of the FWHM. Units aside, the models only populate well-defined regions of the diagram, and, in particular, at ¾ maximum, it is the blueshifted, red asymmetric quadrant into which almost all of the models fall.

Figure 10 may be compared with Figure 1 of Sulentic et al. (1990) to confirm their conclusion. Aside from the excess of radio-loud objects in the redshifted, red asymmetric quadrant of Figure 9, there is no sign of any correlation, or, for the sample as a whole, that any quadrant is preferred. Of course, an analysis such as this cannot rule out a multicomponent model in which a low-amplitude very broad accretion disk contribution is added to a symmetric narrower line.

Whether or not emission from an accretion disk causes the asymmetries, what accounts for the difference between Fe II strong–[O III] weak and Fe II weak–[O III] strong objects? As has been pointed out in past studies which measured line asymmetries, the fact that both redward and blueward asymmetries are seen strongly constrains models (De Robertis 1985; Sulentic 1989). The two most obvious mechanisms for explaining both red and blue asymmetries and their correlation with spectral properties are (1) two competing effects which produce opposite asymmetries (but a small fraction of the emission in the line) and (2) a systematic change in the "obscuration" of the clouds, either individually as a change in optical depth or globally as a change in obscuration by a central disk of clouds on the far side.

Knowing as little as we do about the physical properties of the continuum-emitting and broad-line regions, we can think of several ways to achieve the observed relations. As an example of explanations of the first type, imagine that most of the emission comes from the inner face of infalling material. This produces a blue asymmetry. In objects with thin accretion disks, however, a larger fraction of the material is driven out, perhaps associated with the radio jet that these objects tend to have. These additional clouds add a red asymmetric component. As an example of the second type of explanation, consider a scenario in which the emission comes from the inner faces of outflowing clouds in a toroidal distribution around the accretion disk. This produces a red asymmetric line. As the accretion disk thickens up, observers at most aspect angles will see less and less of the far side clouds, at least those nearest the disk. This will make the line blue asymmetric. A similar effect can be achieved just by changing the optical depth in the lines as the clouds will emit more anisotropically when they are optically thick than when they are thin. Thus, optically thin infalling clouds would produce a red asymmetric profile with a little obscuration of the far side; however, if the clouds become optically thick, the far side clouds could dominate, producing a blue asymmetric line.

4.4. *The Widths of Hβ and He II $\lambda4686$*

There are a number of issues regarding the width of Hβ and He II $\lambda4686$ which can be addressed with this sample. Wandel & Yahil (1985) have proposed that there is a relation between the full width at zero intensity (FWOI) of Hβ and various measures of the luminosity, and they use the assumption of gravitationally bound orbits for the broad emission-line clouds to compute dynamical masses for the objects in their sample. They find a correlation coefficient of 0.50 between FWOI and a $\lambda4000$ continuum luminosity for 94 objects. Such a correlation was *not* seen by Wilkes (1987) whose data consisted of

FWHM measures of the Mg II λ2800 and C IV λ1549 lines and similar monochromatic luminosities. Our data shows a weak correlation ($r = -0.275$) between Hβ FWHM and M_v. Wandel & Yahil (1985) argue that all AGNs are emitting at approximately 1% of the Eddington luminosity; however, their analysis assumes that all objects have about the same covering factor and optical depths in their BLR clouds. In the light of their analysis it is interesting that the steep-spectrum QSOs have larger Hβ FWHM by factors of 2–4 at a given M_v. Using the Wandel & Yahil (1985) assumptions, this would imply that the steep-spectrum objects are emitting at a fraction of their Eddington luminosities 4–16 times lower than the radio-quiet objects with the same optical luminosities.

In those objects for which we were able to measure a FWHM for the He II λ4686 line, it is much broader than Hβ (see Appendix). In a number of other objects, it is clearly very broad, although the signal-to-noise was not sufficient to measure it accurately. This finding is consistent with the work of Osterbrock & Shuder (1982) on lower luminosity AGNs and the work of Mathews & Wampler (1985) and Joly et al. (1985) who compared C IV and Mg II line widths in objects at higher redshift. Given the small sample size, it is impossible to determine any trends involving this quantity, and in particular we note that it is much more difficult to measure the line width in the objects with strong Fe II. Despite this, it is interesting that its width is greater than that of Hβ in every case, and this would argue against models in which a significant fraction of the broadening comes from a process such as electron scattering. Instead, it seems certain that high- and low-ionization lines arise in different clouds, or at least there is a subset of clouds having large velocities which do not emit low-ionization lines.

Finally, we note that in some cases the FW0I of Hβ is extremely large. We have not attempted to measure this parameter because it is quite sensitive to noise and depends strongly on the quality of the Fe II subtraction. In two objects, however, PG 0052+251 and PG 1151+117, both of which have weak Fe II, the red wing of Hβ is visible at large velocities. We measure 35,000 km s^{-1} and 15,700 km s^{-1} for the half-width at zero intensity (HW0I) of these two objects.

5. FUTURE WORK

A number of ideas and explanations for the observed correlations have been proposed above, and some of these are amenable to various tests. In addition, there are a few obvious investigations suggested by the results presented here.

The empirical measurement and removal of Fe II is a powerful technique applied to a long standing problem. Its extension to the UV Fe II transitions would (1) allow comparison of the UV and optical Fe II strengths, (2) allow measurement of Balmer continuum emission, and (3) simplify measurement of Mg II line parameters. Use of a UV spectrum of I Zw 1 for this application is the obvious way to begin.

The ultraviolet, of course, contains much information for confirming or disproving many of the arguments in the discussion above. Investigation of the C III] λ1909 line in these objects could relate the density in the BLR to our eigenvector 1. A comparison of Lyman-α and cleaned Hβ profiles could yield information about the relative optical depths as a function of velocity and could also constrain the explanations for the line asymmetry systematics. The extension of our results on He II to the λ1640 line is another exciting prospect. This line is in a relatively clean spectral region, and a study of its behavior in terms of our analysis ought to be straightforward. In more general terms, it would be interesting to extend our entire method of analysis to the UV, and obtain high quality spectra of the complete sample. Measurement of line strengths and profiles could then be combined with our optical measurements to further constrain the models (or increase the confusion).

Finally, we note that this approach has fairly well defined the first two eigenvectors, but left the next three obscure in terms of connection to physical properties. A larger, complete sample should be analyzed in a similar way to provide information on interpretation of these and on stability of our principal component analysis as a whole. A larger sample also would further populate the flat-spectrum radio-loud subset, and perhaps would show whether they are distinguishable from radio-quiet QSOs.

APPENDIX
NOTES ON INDIVIDUAL OBJECTS

PG 0003+158.—[O III] λ4363 present. FWHM of He II λ4686 is approximately 5800 km s^{-1}.

PG 0003+199.—He I λ4471 and λ5876 present. Bump on red wing of λ 4686 may be He I λ4713.

PG 0026+129.—[O III] λ4363 present. He II λ4686 shows broad and narrow components.

PG 0043+039.—very strong blue asymmetry in Hβ. Broad lump at λ5160 may be due to residual Fe II (42).

PG 0049+171.—[O III] λ4363 present. Hβ has strong narrow component (EW = 12 Å).

PG 0050+124.—Prominent lines at λ5158 and λ5273 identified as [Fe II]. Strong [N II] λ5755 and He I λ5876/Na I λλ5890, 5896 present.

PG 0052+251.—[O III] λ4363 present. If Fe II subtraction is correct, HW0I of Hβ on red side is 35,000 km s^{-1}.

PG 0804+761.—Strong residual Fe II (42).

PG 0921+525.—[O III] λ4363 present. Very broad He I λ4471 visible.

PG 0923+201.—Contamination at λ5600 from second order Mg II λ2800; [O III] λλ4959, 5007 lines are quite blue asymmetric.

PG 0934+013.—[O III] λ4363 present. He II λ4471 present. He II λ4686 has broad and narrow component. FWHM of broad component is 7200 km s^{-1}.

PG 0947+396.—[O III] λλ4959, 5007 lines show strong blue asymmetry.

PG 1011−040.—Very broad He II λ4686.

PG 1012+008.—Very poor Fe II subtraction; [O III] λλ4959, 5007 lines show strong blue asymmetry.

PG 1022+519.—Poor Fe II subtraction. He I λ4471 present. Narrow feature at λ4920 is cosmic ray hit.

PG 1048+342.—[O III] λ4363 present.

PG 1048−090.—Very strong red asymmetry on Hβ.

PG 1049−006.—[O III] λλ4959, 5007 show strong blue asymmetry.

PG 1115+407.—Residual Fe II (42) present.

PG 1116+215.—Poor Fe II subtraction; [O III] λλ4959, 5007 show strong blue asymmetry.

PG 1126−041.—Poor Fe II subtraction; [O III] λλ4959, 5007 show blue asymmetry.

PG 1149−110.—He II λ4471 present; [O III] λ4363 present. FWHM of He II λ4686 broad component is 4500 km s^{-1}.

PG 1151+117.—[O III] lines have blue asymmetry. FW0I of Hβ is very large (HW0I on red side is 15,700 km s^{-1}); [O III] λ4363 present. Some contamination from Mg II λ2800 in second order.

PG 1202+281.—[O III] λ4363 present. Very broad He II λ4686.

PG 1211+143.—Small residual contribution from Fe II (42).

PG 1226+023.—Poor Fe II subtraction. Continuum very bumpy between λ4500 and λ4700 and between λ5100 and λ5700.

PG 1229+204.—Poor Fe II subtraction, particularly in λλ5000–5500 region.

PG 1244+026.—Fe II subtraction not ideal due to very narrow broad lines. Suggestion of very broad He II λ4686 line under component of normal width.

PG 1259+593.—Poor Fe II subtraction. No [O III] lines visible. Obvious lump on blue wing of Hβ—position inconsistent with He II.

PG 1302−102.—[O III] lines show blue asymmetry.

PG 1307+085.—[O III] λ4363 present.

PG 1309+355.—[O III] λ4363 present.

PG 1310−108.—Strong [O III] λ4363 present. FWHM of broad component of He II λ4686 is 5400 km s^{-1}.

PG 1322+659.—FWHM of broad component of He II λ4686 is 5600 km s^{-1}.

PG 1341+258.—Poor Fe II subtraction? Broad wave in λλ5050–5500 region. Extremely broad He II λ4686?

PG 1351+236.—Very peculiar, flat-topped broad-line profile.

PG 1351+640.—[O III] λ4363 present. Hβ shows large bump on blue wing. Despite the fact that Hγ does not appear to show a similar profile in Figure 1, unpublished data (Boroson & Meyers 1991) shows that Hα has an identical bump.

PG 1352+183.—Some residual Fe II (42).

PG 1354+213.—Low signal-to-noise.

PG 1402+261.—No [O III]. Fe II subtraction not ideal due to narrow broad lines. Strongly blue asymmetric Hβ profile.

PG 1404+226.—Fe II subtraction not ideal due to narrow broad lines.

PG 1415+451.—Poor Fe II subtraction.

PG 1416−129.—[O III] λ4363 present.

PG 1425+267.—[O III] λ4363 present.

PG 1427+480.—Some residual Fe II (42).

PG 1435−067.—Some residual Fe II (42).

PG 1440+356.—Fe II subtraction not ideal due to narrow broad lines.

PG 1444+407.—Very broad lump on blue wing of Hβ. Poor Fe II subtraction.

PG 1501+106.—[O III] λ4363 present. FWHM of He II λ4686 is 5900 km s^{-1}.

PG 1512+370.—Narrow feature at λ4594 is cosmic ray hit.

PG 1534+580.—Strong [O III] λ4363 present. FWHM of broad component of He II λ4686 is 6950 km s^{-1}.

PG 1535+547.—Poor Fe II subtraction.

PG 1543+489.—Long tail on blue wing of Hβ.

PG 1552+085.—Poor Fe II subtraction.

PG 1612+261.—[O III] λ4363 present. He II λ4471 present. Small amount of contamination from Mg II λ2800 in second order. FWHM of broad component of He II λ4684 is 6660 km s^{-1}.

PG 1613+658.—[O III] lines show blue asymmetry.

PG 1626+554.—Poor Fe II subtraction especially multiplet 42. Hβ may have very broad base. Small amount of contamination from Mg II λ2800 in second order.

PG 1700+518.—This object is known to be a low-ionization BAL (Turnshek et al. 1985). No [O III] visible. Dip in continuum in range λλ4560–4670 may be broad Hβ absorption. Dip above λ5500 is real and unexplained.

PG 2112+059.—Poor Fe II subtraction. [O III] λ5007 appears to be quite broad.

PG 2130+099.—[O III] lines show blue asymmetry.

PG 2209+184.—Low signal-to-noise data.

PG 2214+139.—Hβ (and Hγ) appear to have secondary sharp peaks at velocity Δv = +1800 km s^{-1}. [O III] lines show blue asymmetry.

PG 2251+113.—He II λ4471 present.

REFERENCES

Baldwin, J. A., Wampler, E. J., & Gaskell, C. M. 1989, ApJ, 338, 630
Barthel, P. D. 1989, ApJ, 297, 621
Bergeron, J., & Kunth, D. 1984, MNRAS, 207, 263
Blandford, R. D., & Rees, M. J. 1978, in Pittsburgh Conference on BL Lac Objects, ed. A. M. Wolfe (Pittsburgh: Univ. Pittsburgh Press), 328
Boroson, T. A., & Meyers, K. A. 1992, in preparation
Boroson, T. A., & Oke, J. B. 1984, ApJ, 281, 535
Boroson, T. A., Persson, S. E., & Oke, J. B. 1985, ApJ, 293, 120
Brown, I. W. A., & Wright, A. E. 1985, MNRAS, 213, 97
Chen, K., Halpern, J., & Filippenko, A. 1989, ApJ, 339, 74
Corbin, M. R. 1990, ApJ, 357, 346
———. 1991, ApJ, 375, 503
De Robertis, M. 1985, ApJ, 289, 67
Dumont, A. M., & Collin-Souffrin, S. 1990, A&AS, 83, 71
Espey, B. R., Carswell, R. F., Bailey, J. A., Smith, M. G., & Ward, M. J. 1989, ApJ, 342, 666
Gaskell, M. 1982, ApJ, 263, 79
Heckman, T. M. 1980, A&A, 88, 311
Hewitt, A., & Burbidge, G. 1987, ApJS, 63, 1
Keel, W. C. 1985, in Astrophysics of Active Galaxies and Quasi-Stellar Objects, ed. J. S. Miller (Mill Valley, CA: University Science Books), 1
Kellermann, K. I., Sramek, R., Schmidt, M., Shaffer, D. B., & Green, R. 1989, AJ, 98, 1195
Kriss, G. 1988, ApJ, 324, 809
Jackson, N., & Browne, I. W. A. 1989, MNRAS, 236, 97
———. 1991, preprint
Jackson, N., Browne, I. W. A., Murphy, D. W., & Saikia, D. J. 1989, Nature, 338, 485
Joly, M. 1991, A&A, 242, 49
Joly, M., Collin-Souffrin, S., Masnou, J. L., & Nottale, L. 1985, A&A, 152, 282
Mathews, W. G., & Wampler, E. J. 1985, PASP, 97, 966

Meyers, K. A., & Peterson, B. M. 1985, PASP, 97, 734
Miley G. K., & Miller, J. S. 1979, ApJ, 228, L55
Mushotzky, R., & Ferland, G. A. 1984, ApJ, 278, 558
Neugebauer, G., Green, R. F., Matthews, K., Schmidt, M., Soifer, B. T., & Bennett, J. 1987, ApJS, 63, 615
Oke, J. B., & Lauer, T. R. 1979, ApJ, 230, 360
Orr, M. J. L., & Browne, I. W. A. 1982, MNRAS, 200, 1067
Osterbrock, D. E. 1977, ApJ, 215, 733
Osterbrock, D. E., & Shuder, J. M. 1982, ApJS, 49, 149
Phillips, M. M. 1976, ApJ, 208, 37
———. 1977, ApJ, 215, 746
———. 1978, ApJ, 226, 736
Scheuer, P. A. G., & Readhead, A. C. S. 1979, Nature, 277, 182
Schmidt, M., & Green, R. F. 1983, ApJ, 269, 352
Setti, G., & Woltjer, L. 1977, ApJ, 218, L33
Steiner, J. E. 1981, ApJ, 250, 469
Sulentic, J. W. 1989, ApJ, 343, 54
Sulentic, J. W., Calvani, M., Marziani, P., & Zheng, W. 1990, ApJ, 355, L15
Tananbaum, H., Avni, Y., Green, R. F., Schmidt, M., & Zamorani, G. 1986, ApJ, 305, 57
Turnshek, D. A., Foltz, C. B., Weymann, R. J., Lupie, O. L., McMahon, R. G., & Peterson, B. M. 1985, ApJ, 294, L1
van Groningen, E. 1984, Ph.D. thesis, Univ. Leiden
Veron-Cetty, M.-P., & Veron, P. 1989, ESO Sci. Rep., No. 7
Wampler, E. J., & Ponz, D. 1985, ApJ, 298, 448
Wandel, A., & Yahil, A. 1985, ApJ, 295, L1
Wilkes, B. J. 1987, in Emission Lines in Active Galactic Nuclei, ed. P. M. Gondhalekar (Chilton, England: Science and Engineering Research Council), 79
Wills, B. J., & Browne, I. W. A. 1986, ApJ, 302, 56